Mapping the Energy and Diffusion Landscapes of Membrane Proteins at the Cell Surface Using High-Density Single-Molecule Imaging and Bayesian Inference: Application to the Multiscale Dynamics of Glycine Receptors in the Neuronal Membrane

Jean-Baptiste Masson,[†‡*] Patrice Dionne,[§¶] Charlotte Salvatico,[‖] Marianne Renner,[‖] Christian G. Specht,[‖] Antoine Triller,[‖*] and Maxime Dahan[§**]

[†]Physics of Biological Systems, Pasteur Institute, Paris, France; [‡]Centre National de la Recherche Scientifique UMR 3525, Paris, France; [§]Laboratoire Kastler Brossel, Centre National de la Recherche Scientifique UMR 8552, Ecole Normale Superieure, Paris, France; [¶]Centre de Recherche Universit Laval Robert-Giffard, Quebec, Canada; [‖]Biologie Cellulaire de la Synapse, Institut National de la Sante et de la Recherche Medicale U1024, Institut de Biologie de l'Ecole Normale Superieure, Paris, France; and **Laboratoire Physico-Chimie, Institut Curie, Centre National de la Recherche Scientifique UMR 168, Universit Pierre et Marie Curie-Paris 6, Paris, France

ABSTRACT Protein mobility is conventionally analyzed in terms of an effective diffusion. Yet, this description often fails to properly distinguish and evaluate the physical parameters (such as the membrane friction) and the biochemical interactions governing the motion. Here, we present a method combining high-density single-molecule imaging and statistical inference to separately map the diffusion and energy landscapes of membrane proteins across the cell surface at ~100 nm resolution (with acquisition of a few minutes). Upon applying these analytical tools to glycine neurotransmitter receptors at inhibitory synapses, we find that gephyrin scaffolds act as shallow energy traps (~3 k_BT) for glycine neurotransmitter receptors, with a depth modulated by the biochemical properties of the receptor-gephyrin interaction loop. In turn, the inferred maps can be used to simulate the dynamics of proteins in the membrane, from the level of individual receptors to that of the population, and thereby, to model the stochastic fluctuations of physiological parameters (such as the number of receptors at synapses). Overall, our approach provides a powerful and comprehensive framework with which to analyze biochemical interactions in living cells and to decipher the multiscale dynamics of biomolecules in complex cellular environments.

INTRODUCTION

Determining the parameters that regulate the mobility of proteins in cells is key for many cellular functions. The motion of proteins depends on a variety of factors, including the local viscosity, their intermittent binding to other proteins, the molecular crowding, and the dimensionality of the accessible space (1). Because all these factors are difficult or impossible to reconstitute in vitro using purified constituents, there is a compelling need for analytical tools that bypass in vitro assays and directly access the properties of macromolecular assemblies and the kinetics of their interactions in their native cellular environment.

Thanks to single-molecule imaging tools, it is now possible to record trajectories of individual proteins in a variety of cellular systems. An important challenge is to extract relevant biochemical and biophysical information from these trajectories. This is commonly done by computing the mean-square displacement (MSD) along the trajectories and estimating the effective diffusion coefficient of the molecule. By associating the diffusional states to the functional states of the biomolecules, one can identify molecular behaviors (1) and evaluate the transition kinetics between them (2). Although this approach has often proved useful, it is conceptually inappropriate in many biological situations. Measuring a diffusion coefficient places emphasis on the friction encountered by the protein and assumes that the movement is characterized by an MSD scaling linearly with time. Yet, the primary factor controlling the motion of a protein is often not the friction but, instead, its interactions with molecular or macromolecular partners leading to transient stabilization or transport. In this case, the relevant information is not the diffusion coefficient but the binding energies between the protein of interest and its interacting partners. Furthermore, regulatory processes are often mediated by changes in these binding energies, which should ideally be evaluated with in situ measurements.

Methods that go beyond the computation of the MSD generally aim to identify deviations from Brownian movement within single-molecule trajectories, due for instance to trapping or transport (3–5). However, these methods essentially remain ad hoc tools and do not constitute a comprehensive framework to describe the parameters underlying the motion. Furthermore, biological media are often spatially inhomogeneous and this heterogeneity is poorly conveyed by measuring a few, sparse trajectories. A conceptually different approach using Bayesian inference methods has been recently proposed to analyze the motion of molecules (6,7). It assumes that the membrane

Submitted July 24, 2013, and accepted for publication October 15, 2013.

*Correspondence: jbmasson@pasteur.fr or triller@biologie.ens.fr or maxime.dahan@curie.fr

Patrice Dionne and Charlotte Salvatico contributed equally to this article.

Editor: Anne Kenworthy.

0006-3495/14/01/0074/10 $2.00

http://dx.doi.org/10.1016/j.bpj.2013.10.027

environment is characterized by two spatially varying quantities:

1. The diffusivity $D(\mathbf{r}) = k_B T/\gamma(\mathbf{r})$ (where $\gamma(\mathbf{r})$ is the local viscosity).
2. The potential energy $V(\mathbf{r})$ that reflects the biochemical interactions of the molecule.

In this framework, the protein is a random walker with a motion governed by the Langevin equation (6),

$$\frac{d\mathbf{r}}{dt} = -\frac{D(\mathbf{r})\nabla V(\mathbf{r})}{k_B T} + \sqrt{2D(\mathbf{r})}\xi(t), \qquad (1)$$

where $\xi(t)$ is a rapidly varying Gaussian noise with zero mean. From a general standpoint, a knowledge of $D(\mathbf{r})$ and $V(\mathbf{r})$, which are protein-specific, can reveal not only how fast the protein moves in the membrane, but also how to identify areas where it can be stabilized (energy traps) or from which it is excluded (energy barriers). However, in the few cases where $D(\mathbf{r})$ and $V(\mathbf{r})$ have been experimentally determined (8,9), the analysis has been limited to movements confined in local regions ($<1\ \mu m^2$), falling short of providing a complete description of the heterogeneous diffusivity and energy landscapes in the cell membrane.

Here, we introduce what we believe to be a novel and generic approach, combining high-density, single-molecule imaging, and computational tools to enable the mapping of the environment of membrane receptors across the entire cell surface and at ~100 nm resolution. This approach allows the mapping of the membrane over regions of several hundred μm^2 in a few minutes of data acquisition. Furthermore, the inferred maps are used to numerically generate massive number of trajectories. These simulated trajectories, whose characteristics match those of the experimental ones, enable a complete analysis of the dynamics in the complex membrane environment by means of various statistical estimators.

To illustrate the relevance and benefits of our approach, we applied it to the neuronal membrane, a cellular system in which the spatial organization is critical for the detection and processing of external information. In past years, tracking experiments have underlined the role of membrane dynamics in ensuring rapid exchange of receptors (e.g., glutamate, glycine, or GABA receptors) between extrasynaptic and synaptic localizations (10). Therefore, the number of receptors at synapses depends on the motion of receptors at the cell surface and their stabilization at synaptic loci, the latter being regulated by the number of scaffolding molecules and the affinity of the receptor-scaffold interactions (11). A quantitative analysis of the protein mobilities and of their regulatory mechanisms is thus paramount for characterizing and modeling the variability of the synaptic response and the plasticity of the nervous system (involved in higher brain functions such as learning and memory or during pathological processes).

MATERIALS AND METHODS

Antibody coupling

Rat anti-GFP monoclonal antibody (Roche Molecular Diagnostics, Pleasanton, CA) was labeled with Atto-647 dye using standard conjugation methods. In brief, 40 μL of antibodies at 0.4 mg/mL in phosphate-buffed saline (PBS) were mixed with 4 μL of 1 M sodium bicarbonate buffer at pH 8.5. This solution was incubated with 10-fold molar excess of Atto-647-NHS-ester (Sigma, St. Louis, MO) diluted at 1 mg/mL in anhydrous dimethyl sulfoxide. After 1 h of incubation at room temperature, the solution was filtered with a Microspin G50 column (GE Healthcare, Little Chalfont, Buckinghamshire, UK) to remove unconjugated dye. The overall coupling efficiency of the dye, estimated by UV-Vis absorption, was ~12%. The labeled antibodies were washed with PBS and concentrated using three rounds of centrifugation with a Vivaspin500 10-kDa cutoff PES membrane filter (GE Healthcare). The concentrated antibody solution was stored at 4°C and used for up to one week.

Cell culture and plasmid transfection

Hippocampal neurons from Sprague-Dawley rats at embryonic day 18 were cultured at a density of 6×10^4 cells/cm^2 on 18-mm coverslips precoated with 80 mg/mL poly-D,L-ornithine (Sigma) and 5% fetal calf serum (Invitrogen, Carlsbad, CA) as described previously in Dahan et al. (19). Cultures were maintained in serum-free neurobasal medium supplemented with 1× B27 and 2 mM glutamine (Invitrogen). Cells were transfected after 6–8 days in vitro using Lipofectamine 2000 (Invitrogen), and imaged 1–2 days after transfection. All coverslips were cotransfected with mRFP-tagged gephyrin and pHluorin-tagged transmembrane (TM) constructs, using 0.4 μg of each plasmid per coverslip. The expression constructs β^{WT}-TM-pHluorin, β^{S403D}-TM-pHluorin, and β^{-}-TM-pHluorin are all described in Specht et al. (12). In brief, β^{S403D} corresponds to the mutation of serine S403 of the GlyRβ subunit that mimics the phosphorylation of the residue by protein kinase C. β^{-}-TM corresponds to the double mutation F398A and I400A of the wild-type GlyR β-loop that abolishes binding to gephyrin.

Cell labeling

Before imaging, we prepared a stock solution of diluted antibodies using casein (Vector Laboratories, Burlingame, CA) as a blocking reagent. We added 2 μL of Atto-647 conjugated anti-GFP antibodies and 10 μL of 10 mg/mL casein to 40 μL of PBS, resulting in an antibody solution of 0.1–0.2 μM. We also prepared a stock of Tetraspeck fluorescent microbeads (Invitrogen) by mixing 1 μL of 0.1 μM microbeads with 400 μL of imaging solution. These multicolor fluorescent beads were used as a reference to align the different imaging channels and to correct for x/y drifts of the stage and the coverslip. The coverslip was mounted in an imaging chamber and incubated with 20 μL of warmed microbead solution for 10 s. After rinsing, the chamber was filled with 600 μL of warmed imaging solution (MEMair: phenol red-free minimum essential medium (MEM), glucose 33 mM, HEPES 20 mM, glutamine 2 mM, Na-pyruvate 1 mM, and B27 1×) and placed on the microscope. To avoid saturating the cell membrane with fluorescent antibodies, we first selected a transfected neuron and added the fluorescent antibodies at a final concentration of 0.3–0.6 nM directly before the start of the acquisition.

Imaging

Measurements were performed on an inverted epi-fluorescence microscope (model No. IX70; Olympus, Melville, NY) equipped with a 100× 1.45NA oil objective and a back-illuminated electron-multiplying charge-coupled device camera (Quantum; Roper Scientific, Trenton, NJ). We imaged the neurons at 37°C in MEMair recording medium using a heated stage. For

each neuron, we first recorded images of the pHluorin signal of the TM constructs and of mRFP-gephyrin fluorescence, using an ultraviolet lamp (Uvico; Rapp OptoElectronic, Wedel, Germany) and standard sets of filters for GFP (excitation 475AF40, dichroic 515DRLP, and emission 535AF45) and RFP (excitation 580DF30, dichroic 600DRLP, and emission 620DF30). Next we acquired a movie in uPAINT (J-T-L Development, http://j-t-l.com/) of the transmembrane proteins labeled with Atto-647-coupled anti-GFP antibodies (20,000 images at 20 frames/s). Atto-647 dyes were excited with a 640-nm laser and their fluorescence was collected through using a 650DRLP dichroic and a 690DF40 emission filter. The laser was tightly focused on the back-focal plane of the objective. The angle of incidence of the beam on the coverslip, controlled by laterally moving the focused spot, was just under the limit of total internal reflection, such that the laser beam in the sample was almost parallel to the glass surface. This angle was slightly adjusted in each experiment to maximize the signal/noise ratio of the single fluorescent spots diffusing in the membrane.

Data analysis

Tracking analysis of the movies was carried out using an adapted version of the multiple target-tracking algorithm (13). In brief, fluorescence spots corresponding to the point-spread function of single emitting fluorophores were fitted with a two-dimensional Gaussian. The center of the fit yielded the position of single molecules with localization accuracy ~30 nm. Trajectories were then computed from individual detections with a nearest-neighbor algorithm.

Simulations in the landscapes

The maps of the diffusion and energy landscapes, $D(\mathbf{r})$ and $V(\mathbf{r})$, can be used to simulate the behavior of the molecules at different time- and space scales. In each mesh subdomain (i, j) a diffusivity $D_{i,j}$ is associated with a potential energy value $V_{i,j}$. The dynamics of the molecules are described by the Fokker-Planck equation

$$\frac{\partial P(\mathbf{r},\mathbf{t}|\mathbf{r}_0,\mathbf{t})}{\partial t} = -\nabla.\left(-\frac{\nabla V(\mathbf{r})P(\mathbf{r},\mathbf{t}|\mathbf{r}_0,\mathbf{t})}{\gamma(\mathbf{r})} - \nabla(D(\mathbf{r})P(\mathbf{r},\mathbf{t}|\mathbf{r}_0,\mathbf{t}))\right), \quad (2)$$

where $P(\mathbf{r}, \mathbf{t}|\mathbf{r}_0, t)$ is the conditional transition probability from $(\mathbf{r}_0, t_0)$ to $(\mathbf{r}, t)$. Fokker-Planck equations can always be approximated by Master equations,

$$\frac{dP_{(i,j)}(t)}{dt} = \sum_{(i',j')\in N(i,j)} W_{(i,j),(i',j')}P_{(i',j')} - \sum_{(i',j')\in N(i,j)} W_{(i',j'),(i,j)}P_{(i,j)}, \quad (3)$$

with, in our case,

$$W_{(i,j),(i',j')} = \frac{D(i',j')}{\Delta x^2}\exp\left(-\frac{\Delta x F^x_{(i,j),(i',j')}}{2\gamma(i',j')D_{(i',j')}}\right), \quad (4)$$

if the transition is in the x direction and a similar formula in the y direction, and with $W_{(i,j),(i',j')}$ as the transition rate from the (i',j') site to the (i, j), Δx (Δy) as the mesh size in the $x(y)$ direction, and with $F^x_{(i,j),(i',j')}$ as the potential gradient acting on the random walker in the x direction when moving from (i, j') to (i, j). Following Eq. 4, the motion of the molecule was simulated using the Gillespie scheme (27). When the molecule was at the site (i, j), the transitions rates, rewritten a_ν to match Gillespie formalism, ν taking values from 1 to 4, were evaluated on all neighboring sites. We define $a_0 = \Sigma_\nu a_\nu$. The time, τ, to move from the site (i, j) to a neighboring site is extracted from an exponential probability density function of rate a_0, so that $\tau = (1/a_0)\log(1/r_1)$ with r_1 a random number in [0,1]. The destination site, k, is chosen to satisfy $\sum_{\nu=0}^{k-1} a_\nu \le r_2 a_0 \le \sum_{\nu=0}^{k} a_\nu$ with r_2 a random number in [0,1]. Limits of the neuronal cells and unvisited sites are defined as inaccessible sites. Note that the trajectory generation process leads to trajectories with non-constant time steps. To evaluate the different estimators, trajectories were regularized to obtain the molecule position at regular time lags by imposing that as long as each τ was not reached, the molecule did not move.

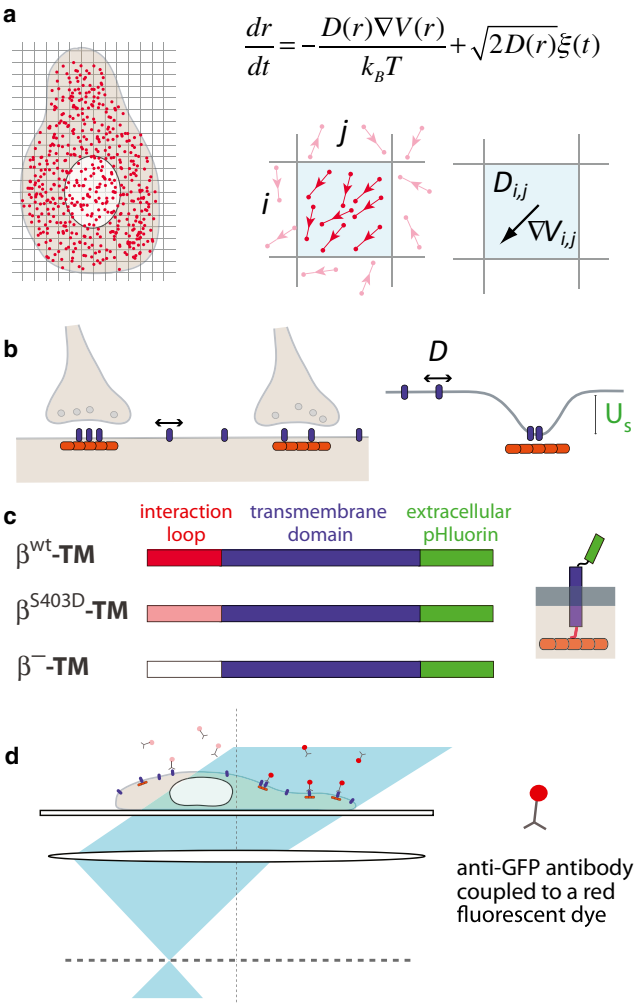

FIGURE 1 General scheme of the assay. (*a*) Principle of the Bayesian inference method. (*Left*) High-density single-molecule data (*red dots*) are recorded at the cell surface. (*Right*) In a mesh domain, multiple translocations (*top*) are used to infer the local diffusivity and force (gradient of the potential) that underlie the motion (*bottom*). (*b*) GlyRs (*blue*) diffuse in the membrane and are in dynamic equilibrium between synaptic and extrasynaptic domains in the neuronal membrane. At synapses, GlyRs are stabilized by their interactions with gephyrin clusters (*orange*), which can be modeled as trapping potential (with depth U_S). (*c*) Expression constructs of transmembrane proteins with an extracellular pHluorin tag and an intracellular interaction loop derived from the GlyR β-subunit. (*d*) Principle of high-density single-molecule uPAINT imaging (16). To see this figure in color, go online.

RESULTS AND DISCUSSION

Mapping the diffusion and energy landscapes with Bayesian inference

Our approach for the large-scale mapping of $D(\mathbf{r})$ and $V(\mathbf{r})$ builds on Bayesian statistical tools recently developed to analyze the motion of individual particles (6,7). The principle of the method is as follows (see details in the Supporting Material): We first acquire high-density single-molecule data (15,16), with a number of individual translocations of 1000–10,000/μm^2. Next, the surface of the cell is meshed with subdomains $S_{i,j}$ (labeled with the index (i,j) along the x and y axis) with a size proportional by a factor δ ~2–3 to the average step size of a translocation, such that consecutive positions of the molecules are either in the same or in adjacent domains (Fig. 1 *a*). From the information contained in the massive number of individual translocations, we determine $D_{i,j}$ and $\nabla V_{i,j}$ in each subdomain (i,j) using Bayesian inference techniques adapted from Türkcan et al. (7). In brief, we compute the global posterior distribution P of the parameters $\{D_{i,j}\}_{(i,j)}$ and $\{\nabla V_{i,j}\}_{(i,j)}$ given the observed trajectories $\{T_k\}_{(k)}$. Since all the subdomains are independent, P is the product of the posterior distributions inside each of them:

$$P\left(\{\nabla V_{i,j}\}_{(i,j)}, \{D_{i,j}\}_{(i,j)} \middle| \{T_k\}_{(k)}\right) = \left(\prod_{(i,j)} P\left(\nabla V_{i,j}, D_{i,j} \middle| \{T_k\}_{(k)}\right)\right) \times P(\nabla V, D) \quad (5)$$

$$\propto \prod_{(i,j)} \left(\prod_{k} \prod_{\mu:\mathrm{r}^{\mathrm{k}}_{\mu} \in \mathrm{S_{i,j}}} \frac{\exp\left(- \frac{\left(\mathrm{r}^{\mathrm{k}}_{\mu+1} - \mathrm{r}^{\mathrm{k}}_{\mu} - \mathrm{D_{i,j}} \nabla \mathrm{V_{i,j}} \Delta \mathrm{t}/\mathrm{k_B T}\right)^2}{4\left(D_{i,j} + \frac{\sigma^2}{\Delta t}\right)\Delta t} \right)}{4\pi\left(D_{i,j} + \frac{\sigma^2}{\Delta t}\right)\Delta t} \times \frac{D_{i,j}^2}{\left(D_{i,j}\Delta t + \sigma^2\right)^2} \right) \quad (6)$$

where μ designates the index for which the points $\mathbf{r}^{\mathrm{k}}{}_{\mu}$ of the k^{th} trajectory are in $S_{i,j}$, the value σ is the experimental localization accuracy (~30 nm), Δt is the acquisition time, and $P(\nabla V, D)$ is the prior information on the potential and the diffusivities. In the second line of Eq. 5, we display the prior we commonly used, Jeffrey's prior, that is discussed in the Supporting Material. The estimators $\{D^{\mathrm{MAP}}_{i,j}, \nabla V^{\mathrm{MAP}}_{i,j}\}_{(i,j)}$ of the local diffusivity and force are the maximum a posteriori of the posterior distribution P (17,18). Finally, we solve the inverse problem to determine in each subdomain the potential field $V_{i,j}$ associated to the force. The estimation of $V_{i,j}$ is performed by minimizing $\xi(\{V_{i,j}\})$, defined as

$$\xi\left(\{V_{i,j}\} \middle| (i,j) \in \{N(i,j)\} \neq 0\right) = \sum_{(i,j)} \left(\nabla V_{i,j} - \nabla V^{\mathrm{MAP}}_{i,j}\right)^2 + \beta(\delta) \sum_{(i,j)} \left(\nabla V_{i,j}\right)^2, \quad (7)$$

with $N(i,j)$ the number of neighboring occupied mesh domains and $\beta(\delta)$ a constant (optimized on numerically generated trajectories) depending on δ (see the Supporting Material). Eventually, the set of quantities $\{D^{\mathrm{MAP}}_{i,j}, \nabla V^{\mathrm{MAP}}_{i,j}\}_{(i,j)}$ constitute the diffusivity and potential energy maps.

Glycine receptors and their interactions with scaffolding proteins

We applied our inference-based mapping method to investigate the dynamics of glycine neurotransmitter receptors (GlyRs) in the neuronal membrane as well as their stabilization at inhibitory synapses (19). This stabilization is achieved through the binding of the receptors to the scaffold protein gephyrin (Fig. 1 *b*) via an intracellular loop (the β-loop) present in the two β-subunits of the pentameric GlyR complex. The high affinity component of the β-loop-gephyrin interaction is in the nanomolar range (K_D~20 nM), as determined by isothermal titration calorimetry (12). To characterize the GlyR-gephyrin interaction in living neurons, we used recombinant membrane proteins consisting of a TM domain and a C-terminal pHluorin tag (a pH-sensitive GFP mutant that is quenched in intracellular acidic vesicular compartments) that were fused N-terminally to the intracellular GlyR β-loop (Fig. 1 *c*). This β^{WT}-TM-pHluorin construct recapitulates the interactions of the endogenous GlyR complexes with the gephyrin scaffold proteins, with the important benefit that individual elements of the receptor-scaffold interaction can be manipulated independently (12). It also overcomes the difficulty of defining the subunit composition of oligomeric receptors where transfected subunits compete with endogenous ones. As a control, we used β^{-}-TM-pHluorin, a construct with a mutated β-loop that does not interact with gephyrin.

High-density single-molecule imaging of TM proteins

We acquired a high density of individual trajectories using uPAINT, a single-molecule movie-making technique in which cells are imaged at an oblique illumination in a buffer containing dye-labeled primary antibodies (16). Because antibodies (in our case, anti-GFP antibodies coupled to Atto647N dyes) continuously bind to their membrane targets, they can be tracked until they either dissociate or photobleach (Fig. 1 *d* and see Movie S1 and Movie S2 in the Supporting Material). Hence, the entire field of view is constantly replenished with new fluorescent labels and a large number of individual trajectories covering a field of view of ~500–1000 μm^2 can be recorded. Experiments were performed on cultured rat hippocampal neurons cotransfected with mRFP-tagged gephyrin and with the pHluorin-tagged transmembrane constructs (Fig. 1 *c*). In typical measurements, movies were recorded for ~5–15 min with an acquisition time $\Delta t = 50$ ms (see Movie S1 and Movie S2), yielding up to hundreds of thousands of individual translocations per field of view, with an average of 30 points per mesh domain (size ~100 × 100 nm^2). On this timescale, the cells and synaptic sites remained relatively stable, meaning that the diffusivity and energy landscapes could be considered constant.

Diffusion and energy maps of TM proteins

Fig. 2, *a–f*, shows examples of the diffusivity and energy maps for the two constructs β^{WT}-TM-pHluorin and β^{-}-TM -pHluorin. In both cases, the diffusion map exhibits fluctuations at short scale (≤ 1 μm or less), with local peaks and valleys and a characteristic diffusivity in the range of 0.05-0.2 $\mu m^2.s^{-1}$ (Fig. 2, *b* and *e*). More striking differences were observed between the energy landscapes. For β^{WT}-TM, the landscape is characterized by the existence of small regions (<0.5 μm^2) corresponding to local energy minima (Fig. 2 *c*). Importantly, gephyrin clusters coincide with energy minima, consistent with the stabilization of the transmembrane proteins at synaptic sites. Yet, we also observed that some other minima did not colocalize with gephyrin clusters, suggesting that β^{WT}-TM-pHluorin might interact

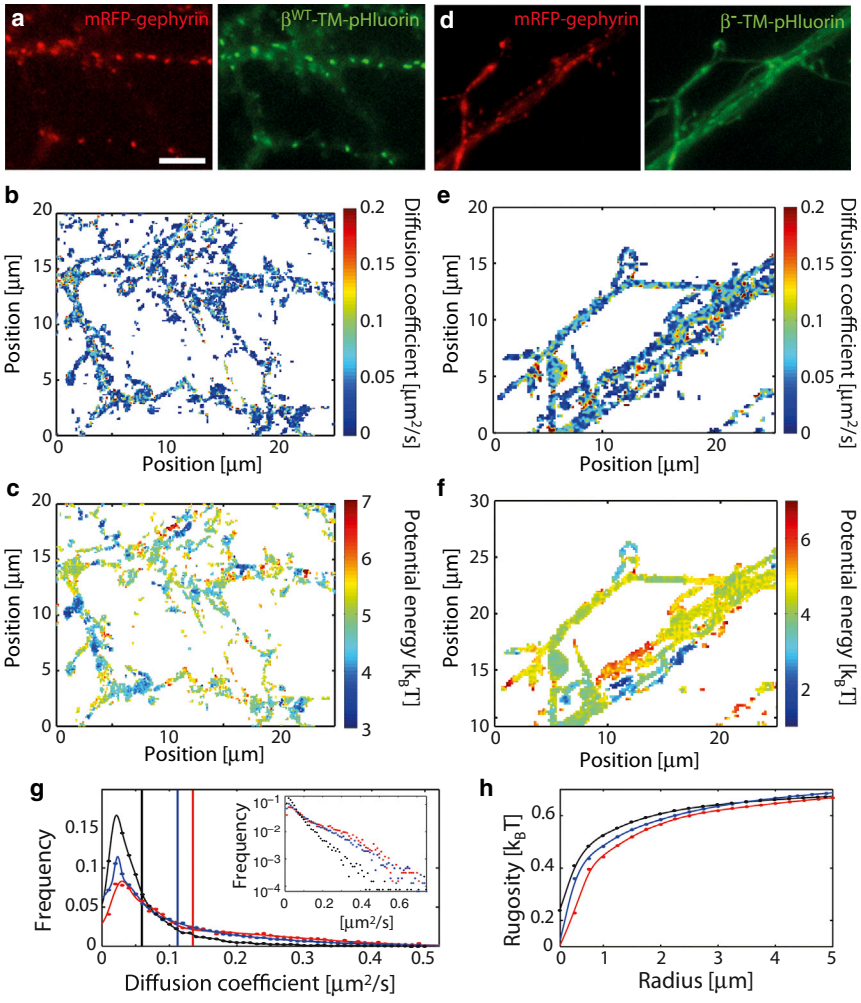

FIGURE 2 Diffusion and energy maps in live neurons. (*a*) Fluorescence images of cultured neurons expressing mRFP-gephyrin and β^{WT}-TM-pHluorin. Scale bar: 10 μm. (*b* and *c*) Diffusion and energy maps. (*d–f*) Equivalent set of images and maps for β^{-}-TM-pHluorin. (*g*) Distribution of diffusion coefficients for the membrane constructs β^{WT}-TM (*black*), β^{S403D}-TM (*blue*), and β^{-}-TM (*red*). (*Vertical bars* on the *x* axis) Mean values of the respective distributions. (*Inset*) Distribution in a lin-log scale. (*h*) Rugosity of the membrane potential as a function of the region radius. To see this figure in color, go online.

with other partners outside of synapses (such as the cytoskeleton or lipid domains). It is possible that these extrasynaptic interactions are still mediated by gephyrin (present in number too small to be detected), because gephyrin is known to associate with GlyRs both inside and outside of synapses (20). In contrast, the energy map for β^{-}-TM (Fig. 2 *f*) shows variations at a longer length-scale, without correlation to gephyrin clusters.

To more quantitatively compare the heterogeneous properties of the neuronal membrane for β^{WT}-TM and β^{-}-TM, we computed two quantities (averaged over seven cells in each case):

1. The distribution of diffusion coefficients in the maps (Fig. 2 *g*), and
2. The rugosity of the energy landscape (Fig. 2 *h* and see the Supporting Material), was defined as the standard deviation of the potential inside an area of defined radius averaged over the complete surface of the cell.

These parameters revealed that the interacting β-loop led to a lower average diffusivity (0.06 $\mu m^2.s^{-1}$ and 0.13 $\mu m^2.s^{-1}$ for β^{WT}-TM and β^{-}-TM, respectively) and a larger rugosity of the potential. This is consistent with the notion that moving TM proteins, when bound to intracellular scaffolding proteins, encounter more obstacles that increase the viscosity of their environment. They are also more likely to interact with membrane or submembrane structures that contribute to the energy landscapes.

Synaptic scaffolds as crowded energy traps

Given the pronounced differences between the energy landscapes of the β^{WT}-TM and β^{-}-TM constructs, we examined the behavior of β^{WT}-TM at gephyrin clusters in closer details. An example of the energy profile of β^{WT}-TM proteins at a synaptic cluster (identified by the presence of mRFP-gephyrin fluorescence) is shown in Fig. 3 *a*. The profile reinforces the view that clusters of scaffolding proteins act as energy traps for membrane receptors (9,10,19). The average trap depth was 3.6 ± 0.4 k_BT (mean ± SE, n = 69 clusters), a relatively shallow potential from which receptors can escape rapidly. Yet, ~15% of clusters had stabilization energies greater than 6 k_BT, corresponding to a much more stable anchoring of receptors (Fig. 3 *b*). This reflects the heterogeneity of the synaptic domains in the neuronal membrane and underlines the need for measurements at the single synapse level.

Of note, the binding energies between β^{WT}-TM and gephyrin seem to be significantly lower than the stabilization energy of AMPA receptors at synaptic sites, for which 25% of the wells had a depth larger than 8 k_BT (9). The method used in Hoze et al. (9), also based on a combination of high-density single-molecule imaging and statistical inference, evaluates the diffusion and drift by computing the maximal likelihood estimation in a mesh square as described in Türkcan et al. (7). The confining potentials were subsequently evaluated by L2 minimization of a parabolic-shaped potential from the force (drift) fields. In Hoze

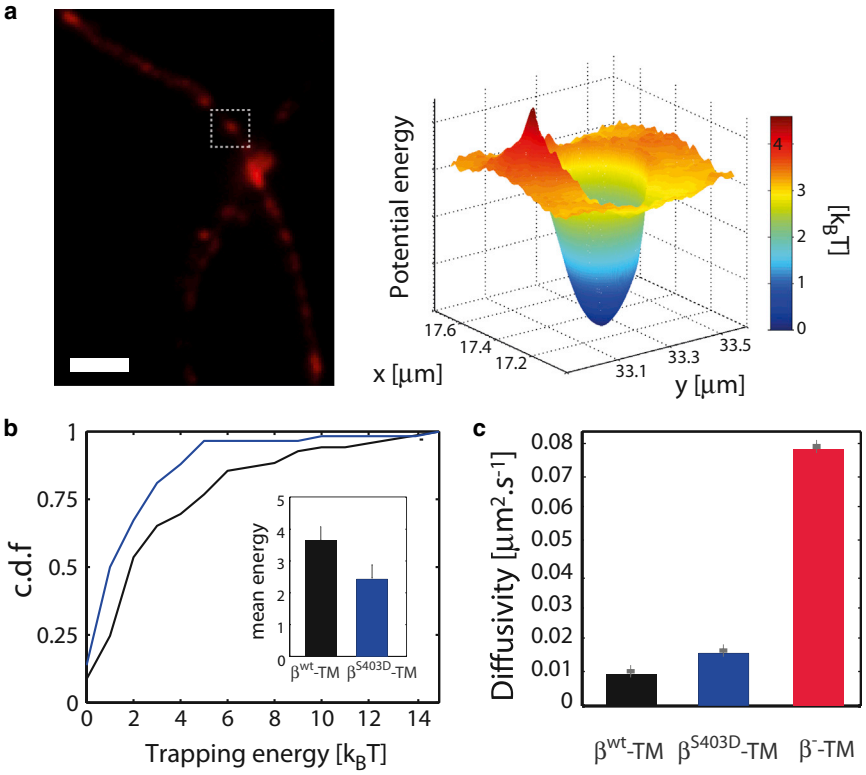

FIGURE 3 Analysis of the synaptic gephyrin scaffold. (*a*) Example of a gephyrin cluster (indicated by a *box*) acting as a local trap in the energy landscape. Scale bar: 5 μm. (*b*) Cumulative distribution function of trapping energy for the constructs β^{WT}-TM (*black*) and β^{S403D}-TM (*blue*). (*Inset*) Mean values of the distribution. Error bars indicate the mean ± SE. (*c*) Mean diffusivity for β^{WT}-TM (*black*), β^{S403D}-TM (*blue*), and β^{-}-TM (*red*). Error bars indicate the mean ± SE. To see this figure in color, go online.

et al. (9) the authors do not discuss the role of known biases with confining potentials (see (7,8,21)) or the effect of the positioning noise, and do not provide information on the posterior distribution of the parameters. It is thus difficult to precisely compare their experimental results with ours. Yet, given that the diffusivity of AMPARs at excitatory synapses appears to be higher than the diffusivity of GlyRs at inhibitory synapses (gephyrin clusters), higher confining potentials may be necessary to stabilize the AMPARs. In addition, we noticed that the average diffusivity of β^{WT}-TM (~0.01 $\mu m^2.s^{-1}$) inside gephyrin clusters was reduced by a factor ~6 compared to extrasynaptic regions (Fig. 3 *c*), probably due to the combined effect of membrane crowding within synaptic sites and the binding to scaffolding elements. In comparison, the diffusivity of β^{-}-TM proteins inside gephyrin clusters, which we expect to be predominantly influenced by molecular crowding (22), was 0.07 $\mu m^2.s^{-1}$ (Fig. 3 *c*), only a factor ~2 lower than in extrasynaptic domains. In other words, the synaptic scaffold stabilizes the receptor by simultaneously diminishing the diffusivity of the receptor and by acting as a trapping potential.

Modulation of the β-loop gephyrin binding affinity

Because the computation of the energy landscape allows the unambiguous distinction between interacting membrane constructs and those lacking interaction domains, we tested the sensitivity of our approach with the phosphomimetic construct β^{S403D}-TM, a mutated β-loop known to have a lower gephyrin binding affinity in vitro (K_D ~0.9 μM (12)) (Fig. 1 *c*). As a result, β^{S403D}-TM displayed increased membrane diffusion and reduced synaptic accumulation compared to β^{WT}-TM. The phosphorylation of the amino-acid residue S403 of the GlyRβ subunit by protein kinase C thus contributes to the regulation of GlyR levels at inhibitory synapses (12). The diffusion and energy landscapes of β^{S403D}-TM (computed over six different cells) yielded a diffusivity (average value 0.11 $\mu m^2.s^{-1}$) and an energetic rugosity precisely intermediate between those of the wild-type and of the binding-deficient constructs (Fig. 2, *g* and *h*). Compared to β^{WT}-TM, the average trap depth of β^{S403D}-TM at synaptic sites was reduced to 2.4 $\pm$ 0.4 k_BT (n = 58 clusters), with less than 5% of the traps above 6 k_BT (Fig. 3 *b*). Inside clusters, the average diffusivity (0.015 $\mu m^2.s^{-1}$) was slightly higher than for the wild-type (Fig. 3 *c*).

Importantly, the binding energy reported here corresponds to TM proteins moving in a two-dimensional membrane and interacting with macromolecular gephyrin scaffolds that are believed to be two-dimensional as well (23,24). This is in contrast with measurement of the equilibrium constant K_D by isothermal calorimetry, which reports on the individual interaction between the β-loop and the scaffolding protein in an isotropic, three-dimensional measurement of the β-loop-scaffold interaction. Obtaining the stabilization energy thus constitutes a first and important step to bridge the gap between in vitro and in situ biochemical measurements. When further complemented with data on the ultrastructure and stoichiometry of synaptic scaffolds (that are now accessible with single-molecule imaging techniques (24,25)), we expect our approach to enable a true determination of the two-dimensional affinity of the membrane proteins for the synaptic scaffolds (26).

Connecting the landscapes and the global mobility of proteins

An important question for the dynamics of proteins is how the variability of their diffusion and energy landscapes at short scale (~100 nm) affects their long-distance mobility and, thereby, the kinetics of many intermolecular reactions. Reaching a multiscale description of the motion in the membrane has long been a challenge in single-molecule experiments. High-density sampling is usually achieved with poorly stabilized probes, yielding numerous but short trajectories (15,16). In contrast, long trajectories obtained with more stable markers such as quantum dots (27) only provide a sparse sampling of the cell surface. Furthermore, the nature of the motion, such as subdiffusion, may prevent efficient space sampling with single long trajectories. Here, we adopted a different strategy and used the inferred maps as phenomenological templates to simulate the motion of proteins. Practically, we used the Gillespie scheme (31) to generate individual trajectories lasting up to 500 s (see Materials and Methods and the Supporting Material).

From a large number of simulated trajectories, we could compute ensemble-averaged quantities. We first evaluated the propagator $\Pi(d, t)$, namely the probability density function of moving a distance d in a time t, which is the fundamental estimator characterizing the random motion in a complex environment (28). Although the difference in the average trapping energy at gephyrin clusters was only ~1 k_BT between β^{WT}-TM and β^{S403D}-TM, it led to significant changes in the mobility, reducing the probability of moving over long distances with increasing strength of the β-loop-gephyrin interaction (Fig. 4 *a*). To more carefully examine the nature of the movement of β^{WT}-TM, we plotted $\Pi(d, t)$, at different times t. The curves could be approximated by Gaussian curves $\exp(-d^2/2\chi^2(t))$ with $\chi(t) \propto t^{\alpha}$ and $\alpha = 0.33$, less than 0.5 the value expected for a standard Brownian motion (Fig. 4, *b* and *c*). In fact, these results are consistent with a subdiffusive movement resulting from a fractional Brownian motion due to heterogeneities in the diffusion and energy landscapes (28). Similar results were obtained for β^{S403D}-TM and β^{-}-TM, with α increasing to 0.39 and 0.41, respectively (Fig. 4 *c*). The subdiffusive nature of the motion could be further illustrated

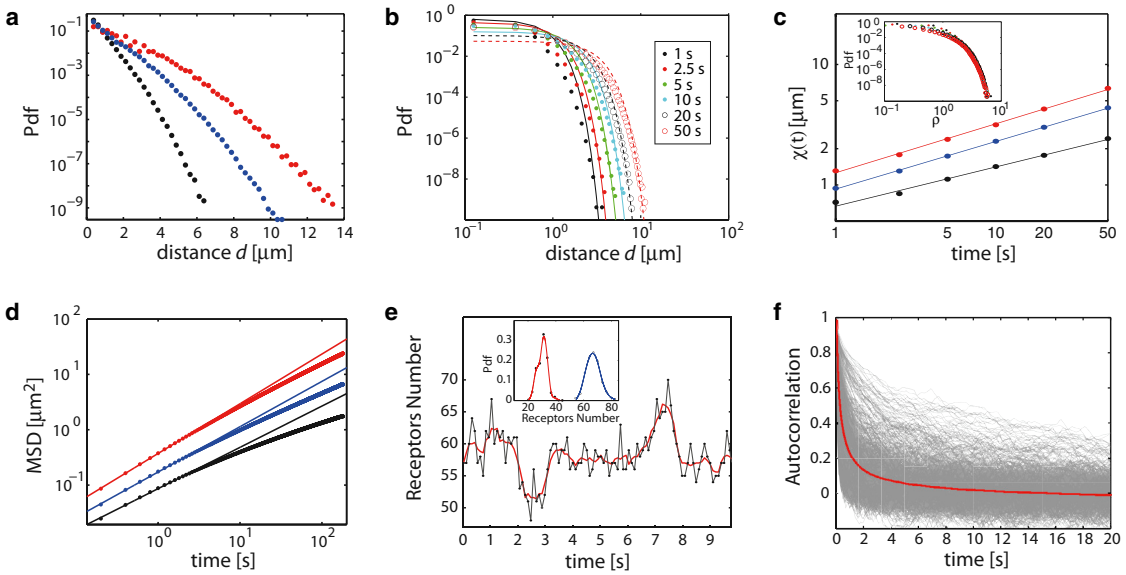

FIGURE 4 Analysis of simulated trajectories in the inferred maps. Unless otherwise mentioned, the results correspond to the constructs β^{WT}-TM (*black*), β^{S403D}-TM (*blue*), and β^{-}-TM (*red*). (*a*) Ensemble-averaged propagator $\Pi(d, t)$, defined as the probability density function to move by a given distance in $t =$ 10 s. (*b*) Propagator $\Pi(d, t)$ for the construct β^{WT}-TM computed at different times t. (*Plain lines*) Adjustments with the Gaussian curves $\exp(-d^2/2\chi^2(t))/2\pi\chi^2(t)$. (*c*) Curves $\chi(t)$. (*Inset*) Propagators for the construct β^{WT}-TM as a function of the rescaled variable $\rho = d/\chi(t)$. (*d*) Mean-squared displacement as a function of time. (*Straight lines*) Subdiffusive behavior at short timescales. (*e*) Time-course of the number of receptors at a single synapse. (*Inset*) Distribution of the minimum (in *red*) and maximum (in *blue*) number of receptors computed over traces of 300 s for all the gephyrin clusters. (*f*) Autocorrelation functions (in *gray*) for the time traces of number of receptors at gephyrin clusters (computed over 300 s). (*Red line*) Average autocorrelation function. To see this figure in color, go online.

by computing the ensemble-averaged MSD for the three transmembrane constructs (Fig. 4 *d*). On the timescales 0.05–5 s, all the MSDs increased sublinearly, with an anomalous exponent α equal to 0.75, 0.82, and 0.89 for β^{WT}-TM, β^{S403D}-TM, and β^{-}-TM, respectively. The MSD anomalous exponents are slightly larger than 2α, likely due to boundary effects associated to the size and geometry of the neurons.

Finally, we examined the implications of the local properties of the mobility of individual GlyRs on their global distribution in the membrane and on the receptor occupancy at synapses. To do so, we simulated the membrane dynamics of a population of receptors, using surface densities derived from prior experimental reports (see the Supporting Material). We computed in particular the time course of the number of receptors at individual synaptic clusters, which we expect to fluctuate due to the exit and entry fluxes of receptors (Fig. 4 *e* and see the Supporting Material). The exit kinetics at a given synapse is determined by the shape and amplitude of the trapping potential combined with the reduced diffusivity in the cluster. In contrast, the entry kinetics depends on the motion of all the receptors over the entire cell surface and need to be computed using the diffusion and energy maps. The number of receptors varied significantly over times, as illustrated by the distribution of their minimal and maximal numbers at individual synapses (Fig. 4 *e*). Furthermore, the timescale of these fluctuations, analyzed by computing the autocorrelation function, is comprised between ~1 s and a few tens of seconds, showing a large heterogeneity among gephyrin clusters (Fig. 4 *f*). These observations may account for the dynamic range of receptor numbers at synapses and for the variability of synaptic transmission (29). The receptor fluctuations, which are equivalent to a noise, may also favor the transition from one steady state to another during synaptic plasticity (29,30).

CONCLUSION

The motion of proteins in the plasma membrane is influenced by both a viscous landscape, $\gamma(\mathbf{r})$, and an interaction potential, $V(\mathbf{r})$. We have introduced a method to map the interaction energy and diffusion landscapes in the cellular membrane with ~100 nm resolution over surfaces of several hundred μm^2. The possibility of simulating trajectories in the inferred maps offers many possibilities to address the multiscale dynamics of membrane proteins. In particular, it bridges the gap between the information obtained from numerous, dense—but short—trajectories acquired using uPAINT (15) or single-particle tracking PALM techniques (14), and that from the much longer, but usually sparse, trajectories extracted through the tracking of proteins labeled with photostable fluorophores

(Qdots, nanoparticles). These trajectories can be used to accurately evaluate various statistical estimators, thus enabling the analysis of the dynamics of biomolecules in complex media.

We anticipate that our method will be instrumental to identify the factors governing the mobility of specific molecules (such as friction, molecular interactions and geometry of the cell) and thereby to model and analyze reaction-diffusion processes in biological media. As illustrated in the case of GlyR-gephyrin binding, it also paves the way to in situ biochemical measurements, which is key for a quantitative analysis of the regulation of molecular interactions in a cellular environment. Our approach should also be helpful to describe the molecular noise that results from variability of protein concentrations across the cell surface and may play an important role in information processing at the single cell level (29). Beyond the case of receptor-scaffold interactions, our analytical tools can be applied to other biological questions, such as the stability of macromolecular assemblies in the cytoplasm or the nucleus, or to the sequence-dependent movement of proteins along DNA (32).

SUPPORTING MATERIAL

Eight figures, 25 equations, and two movies are available at http://www.biophysj.org/biophysj/supplemental/S0006-3495(13)01194-6.

We are grateful to Paul de Koninck for his support and discussion. We also thank Diego Krapf for his critical reading of the paper and multiple suggestions.

This work was funded by Centre National de la Recherche Scientifique, Institut National de la Santé et de la Recherche Médicale; C'Nano Ile de France, the program "Prise de Risque" from the Centre National de la Recherche Scientifique; Agence Nationale pour la Recherche PiriBio; the grant Synaptune from the Agence Nationale pour la Recherche; program No. ANR-10-IDEX-0001-02 PSL; and the state program Investissements d'Avenir managed by Agence Nationale de la Recherche (grant No. ANR-10-BINF-05 "Pherotaxis").

REFERENCES

1. Saxton, M. J., and K. Jacobson. 1997. Single-particle tracking: applications to membrane dynamics. *Annu. Rev. Biophys. Biomol. Struct.* 26:373–399.
2. Persson, F., M. Lindén, …, J. Elf. 2013. Extracting intracellular diffusive states and transition rates from single-molecule tracking data. *Nat. Methods.* 10:265–269.
3. Simson, R., E. D. Sheets, and K. Jacobson. 1995. Detection of temporary lateral confinement of membrane proteins using single-particle tracking analysis. *Biophys. J.* 69:989–993.
4. Huet, S., E. Karatekin, …, J. P. Henry. 2006. Analysis of transient behavior in complex trajectories: application to secretory vesicle dynamics. *Biophys. J.* 91:3542–3559.
5. Bouzigues, C., and M. Dahan. 2007. Transient directed motions of $GABA_A$ receptors in growth cones detected by a speed correlation index. *Biophys. J.* 92:654–660.
6. Masson, J. B., D. Casanova, …, A. Alexandrou. 2009. Inferring maps of forces inside cell membrane microdomains. *Phys. Rev. Lett.* 102:048103.
7. Türkcan, S., A. Alexandrou, and J.-B. Masson. 2012. A Bayesian inference scheme to extract diffusivity and potential fields from confined single-molecule trajectories. *Biophys. J.* 102:2288–2298.
8. Türkcan, S., M. U. Richly, …, J. B. Masson. 2013. Probing membrane protein interactions with their lipid raft environment using single-molecule tracking and Bayesian inference analysis. *PLoS ONE.* 8:e53073.
9. Hoze, N., D. Nair, …, D. Holcman. 2012. Heterogeneity of AMPA receptor trafficking and molecular interactions revealed by superresolution analysis of live cell imaging. *Proc. Natl. Acad. Sci. USA.* 109:17052–17057.
10. Triller, A., and D. Choquet. 2008. New concepts in synaptic biology derived from single-molecule imaging. *Neuron.* 59:359–374.
11. Renner, M. L., L. Cognet, …, D. Choquet. 2009. The excitatory postsynaptic density is a size exclusion diffusion environment. *Neuropharmacology.* 56:30–36.
12. Specht, C. G., N. Grünewald, …, A. Triller. 2011. Regulation of glycine receptor diffusion properties and gephyrin interactions by protein kinase C. *EMBO J.* 30:3842–3853.
13. Sergé, A., N. Bertaux, …, D. Marguet. 2008. Dynamic multiple-target tracing to probe spatiotemporal cartography of cell membranes. *Nat. Methods.* 5:687–694.
14. Risken, H. 1997. The Fokker-Planck Equation: Methods of Solutions and Applications. Springer, New York.
15. Manley, S., J. M. Gillette, …, J. Lippincott-Schwartz. 2008. High-density mapping of single-molecule trajectories with photoactivated localization microscopy. *Nat. Methods.* 5:155–157.
16. Giannone, G., E. Hosy, …, L. Cognet. 2010. Dynamic superresolution imaging of endogenous proteins on living cells at ultra-high density. *Biophys. J.* 99:1303–1310.
17. MacKay, D. J. C. 2003. Information Theory, Inference, and Learning Algorithms. Cambridge University Press, Cambridge, UK.
18. von Toussaint, U. 2011. Bayesian inference in physics. *Rev. Mod. Phys.* 83:943–999.
19. Dahan, M., S. Lévi, …, A. Triller. 2003. Diffusion dynamics of glycine receptors revealed by single-quantum dot tracking. *Science.* 302:442–445.
20. Ehrensperger, M. V., C. Hanus, …, M. Dahan. 2007. Multiple association states between glycine receptors and gephyrin identified by SPT analysis. *Biophys. J.* 92:3706–3718.
21. Voisinne, G., A. Alexandrou, and J.-B. Masson. 2010. Quantifying biomolecule diffusivity using an optimal Bayesian method. *Biophys. J.* 98:596–605.
22. Renner, M., D. Choquet, and A. Triller. 2009. Control of the postsynaptic membrane viscosity. *J. Neurosci.* 29:2926–2937.
23. Fritschy, J. M., R. J. Harvey, and G. Schwarz. 2008. Gephyrin: where do we stand, where do we go? *Trends Neurosci.* 31:257–264.
24. Specht, C. G., I. Izeddin, …, A. Triller. 2013. Quantitative nanoscopy of inhibitory synapses: counting gephyrin molecules and receptor binding sites. *Neuron.* 79:308–321.
25. Lord, S. J., H. L. Lee, and W. E. Moerner. 2010. Single-molecule spectroscopy and imaging of biomolecules in living cells. *Anal. Chem.* 82:2192–2203.
26. Wu, Y., J. Vendome, …, B. Honig. 2011. Transforming binding affinities from three dimensions to two with application to cadherin clustering. *Nature.* 475:510–513.
27. Pinaud, F., S. Clarke, …, M. Dahan. 2010. Probing cellular events, one quantum dot at a time. *Nat. Methods.* 7:275–285.
28. Metzler, R., and J. Klafter. 2004. The restaurant at the end of the random walk: recent developments in fractional dynamics descriptions of anomalous dynamical processes. *J. Phys. A.* 37:R161.

29. Ribrault, C., K. Sekimoto, and A. Triller. 2011. From the stochasticity of molecular processes to the variability of synaptic transmission. *Nat. Rev. Neurosci.* 12:375–387.

30. Sekimoto, K., and A. Triller. 2009. Compatibility between itinerant synaptic receptors and stable postsynaptic structure. *Phys. Rev. E Stat. Nonlin. Soft Matter Phys.* 79:031905.

31. Gillespie, D. 1977. Exact stochastic simulation of coupled chemical reactions. *J. Phys. Chem.* 81:2340–2361.

32. Leith, J. S., A. Tafvizi, …, A. M. van Oijen. 2012. Sequence-dependent sliding kinetics of p53. *Proc. Natl. Acad. Sci. USA.* 109:16552–16557.

Supplementary Information

Mapping the energy and diffusion landscapes of membrane receptors at the cell surface using high-density single-molecule imaging and Bayesian inference

J.-B. Masson[1,2], P. Dionne[‡3,4*], C. Salvatico[‡5*], M. Renner[5], C.G. Specht[5], A. Triller[5] and M. Dahan[3,6]

1 Institut Pasteur, Physics of Biological Systems, 28 rue du Dr Roux, 75724, Paris Cedex 15, France.

2 CNRS, URA 2171, F-75015 Paris, France.

3 Laboratoire Kastler Brossel, Centre National de la Recherche Scientifique UMR8552, Ecole normale supérieure, Université Pierre et Marie Curie-Paris 6, 75005 Paris, France;

4 Centre de Recherche Universite Laval Robert-Giffard, Quebec, Canada.

5 Biologie Cellulaire de la Synapse, Institut Nationale de la Santé et de la Recherche Médicale U789, Ecole normale supérieure, 75005 Paris, France.

6 Present address: Laboratoire Physico-Chimie, Institut Curie, CNRS UMR168, Paris France

* These authors contributed equally

1. Elements on the inference scheme

General Procedure of the Bayesian inference. The inference scheme features two generic steps: first, the derivation of the *posteriori* probability distribution of the unknown parameters given the experimental observations and second the sampling of the posterior distribution to estimate the parameters. It follows from Bayes rule that the posterior probability distribution $P(\{U_l\}|\{T_k\})$ of the set of the unknown parameters $\{U_l\}$ given the set of observed trajectories $\{T_k\}$ reads

$$P\left(\{U_l\}|\{T_k\}\right)=\frac{P\left(\{T_k\}|\{U_l\}\right)P\left(\{U_l\}\right)}{P\left(T_k\right)} \quad \text{(S1)}$$

where $P(\{T_k\}|\{U_l\})$ is the likelihood of the trajectories given the set of parameters $\{U_l\}$, $P(\{U_l\})$ is the prior probability of the set of parameters and $P(\{T_k\})=\int P(\{T_k\}|\{U_l\})P(\{U_l\})d\{U_l\}$ is the evidence of the model. Without any prior knowledge we used Jeffrey's prior as a prior distribution (discussed below). The estimator of the set of parameters $\{U_l\}$ (in this paper) is the Maximum A Posteriori (MAP), *i.e.* the values of $\{U_l\}$ that maximize the posterior distribution.

Prior Information. There are various choices of priors for the inference depending on its expression and on what characteristics of the diffusion and potential fields are to be extracted.

Jeffrey's rule: Results displayed in the paper were inferred using the following prior. Experimentally, there are no prior information on the diffusion and potential fields. Yet, in Bayesian inference, prior knowledge can be extracted from the symmetries of the likelihood distribution [1]. Jeffrey's rule states that:

$$P\left(\{U\}\right)\propto\sqrt{|J|} \quad \text{(S2)}$$

where J is the matrix defined by

$$J = \left(\partial_U \partial_{U'}^T \int d\mathbf{r} \sqrt{P\left(\mathbf{r}|\{U\}\right) P\left(\mathbf{r}|\{U'\}\right)} \right)_{U=U'} \tag{S3}$$

and ∂_U is the gradient with respect to the components U_l of the N-dimensional hypothesis

$$\partial_U = \begin{pmatrix} \partial/\partial U_1 \\ \cdot \\ \cdot \\ \partial/\partial U_N \end{pmatrix} \tag{S4}$$

with N the total number of parameters. The operator $\partial_U \partial_{U'}^T$ is the dyadic product of the gradients, *i.e.* the matrix of the second derivatives. Note that $\sqrt{|J|}$ is proportional to the Fisher Information of the likelihood [2,3].

Inside a mesh domain the likelihood reads

$$P\left(\Delta\mathbf{r}, \Delta\mathbf{t} \middle| D_{i,j}, \nabla_x V_{i,j}, \nabla_y V_{i,j}\right) =$$

$$\frac{1}{4\pi\left(D_{i,j} + \frac{\sigma^2}{\Delta t}\right)\Delta t} \exp\left(-\frac{\left(\Delta x - D_{i,j}\nabla_x V_{i,j}/k_B T\right)^2}{4\left(D_{i,j} + \frac{\sigma^2}{\Delta t}\right)\Delta t} - \frac{\left(\Delta y - D_{i,j}\nabla_y V_{i,j}/k_B T\right)^2}{4\left(D_{i,j} + \frac{\sigma^2}{\Delta t}\right)\Delta t} \right) \tag{S5}$$

where all the sources of positioning noise, such as Poisson noise, background fluorescence, algorithm to fit the intensity profile… are modelled into one Gaussian distribution with null average and σ standard deviation. This leads to the prior

$$P\left(D_{i,j}, \nabla_x V_{i,j}, \nabla_y V_{i,j}\right) \propto \frac{D_{i,j}^2}{\left(D_{i,j}\Delta t + \sigma^2\right)^2} \tag{S6}$$

An example of prior is plotted in Fig. S1:

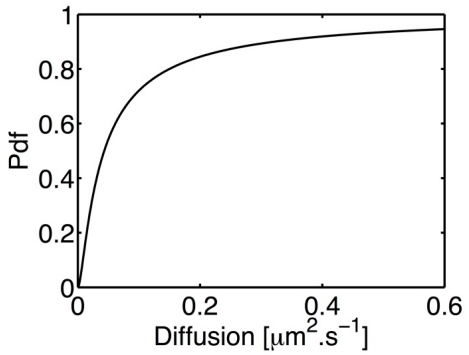

Figure S1. Prior distribution of the parameters with Δt= 0.05s and σ= 30nm. The Prior distribution cannot be normalized.

Interestingly, this prior is still improper (it cannot be normalized) and if there were no positioning noise the prior would be flat which would lead to maximum likelihood optimization for the estimation of the diffusion and potential fields.

The smoothing prior: In the version of the inference scheme used in the analysis of the data, high gradient damping is introduced in the potential optimization scheme. It was also possible to introduce it directly, through a prior penalizing high gradients values:

$$P\left(\left\{\nabla V_{i,j}\right\}_{(i,j)=(1..n_x,1..n_y)},\left\{D_{i,j}\right\}_{(i,j)=(1..n_x,1..n_y)}\middle|\left\{T_l\right\}\right)=\prod_{(i,j)=(1..n_x,1..n_y)}P\left(\nabla V_{i,j},D_{i,j}\middle|\left\{T_l\right\}\right)\times P(\nabla V)$$

$$\propto\prod_{(i,j)=(1..n_x,1..n_y)}\prod_{\mu:r_\mu\in S_{i,j}}\frac{e^{\left(-\left(\mathbf{r}_{\mu+1}-\mathbf{r}_\mu-D_{i,j}\nabla V_{i,j}\Delta t_\mu/k_BT\right)^2\Big/4\left(D_{i,j}+\frac{\sigma^2}{\Delta t_\mu}\right)\Delta t_\mu\right)}}{4\pi\left(D_{i,j}+\frac{\sigma^2}{\Delta t_\mu}\right)\Delta t_\mu}\times e^{\left(-\beta\left\|\nabla V_{i,j}\right\|^2\right)} \tag{S7}$$

It is worth noting that in that case, the potential evaluation could be performed by minimizing:

$$\xi\left(\left\{V_{i,j}\right\}\middle|(i,j)\in\left\{\left|N(i,j)\right|\neq 0\right\}\right)=\sum_{(i,j)}\left(\nabla V_{i,j}-\nabla V_{i,j}^{\inf}\right)^2 \tag{S8}$$

For our measurements, the two damping methods led to similar results.

Experimental Prior: Experimental data accumulated on various cells can be used as priors for future inference. Statistics of diffusion values in the mesh cells can be used as a global prior on diffusion values. Similarly, the smoothness of the diffusion and potential fields can be extracted from experimental data by fitting the distribution of $\left\|\nabla V_{i,j}\right\|^2$ and $\left\|\nabla D_{i,j}\right\|^2$ with the distribution $p_\beta(x)=e^{-\beta x}$ to find the optimal β_{opt} and then use $p_{\beta_{opt}}$.

Likelihood of the diffusivity and gradient potential over the cell surface. The local surface of the cell is meshed with regular subdomains whose dimensions are proportional to the average jump lengths. The typical length of the subdomains is designed so that the biomolecule motion between two consecutive frames happens either inside the same mesh subdomain or between two nearing subdomains. Note that nothing prevents irregular meshing of the surface of the cell, as long as there is no undersampling of internal mesh rectangles. Within each mesh subdomain the potential gradient is approximated to be constant. So inside the mesh square *(i,j)* the solution of Fokker-Planck equation reads

$$P\left(\mathbf{r},t\middle|\mathbf{r}_0,t_0\right)=\frac{e^{\left(-\left(\mathbf{r}-\mathbf{r}_0-D_{i,j}(\nabla V)_{i,j}(t-t_0)\right)/k_BT\right)^2\Big/4\left(D_{i,j}+\frac{\sigma^2}{(t-t_0)}\right)(t-t_0)\right)}}{4\pi\left(D_{i,j}+\frac{\sigma^2}{(t-t_0)}\right)(t-t_0)} \tag{S9}$$

As all the mesh domains are independent, the global posterior distribution *P* is the product of the posteriori inside each of them [4]:

$$P\left(\left\{\nabla V_{i,j}\right\}_{(i,j)=(1..n_x,1..n_y)},\left\{D_{i,j}\right\}_{(i,j)=(1..n_x,1..n_y)}\middle|\left\{T_l\right\}\right)=\prod_{(i,j)}P\left(\nabla V_{i,j},D_{i,j}\middle|\left\{T_l\right\}\right)$$

$$=\prod_{(i,j)}\left(\prod_{l}\prod_{\mu:\mathbf{r'}_\mu\in S_{i,j}}\frac{\exp\left(-\left(\mathbf{r'}_{\mu+1}-\mathbf{r'}_\mu-D_{i,j}\nabla V_{i,j}\Delta t/k_BT\right)^2\Big/4\left(D_{i,j}+\frac{\sigma^2}{\Delta t}\right)\Delta t\right)}{4\pi\left(D_{i,j}+\frac{\sigma^2}{\Delta t}\right)\Delta t}\right) \tag{S10}$$

where μ designates the index for which the points $\mathbf{r}^{l}_{\mu}$ of trajectory l are in $S_{i,j}$, σ is the experimental localization accuracy (~30 nm) and Δt the acquisition time. The estimators $\left(D^{\mathrm{MAP}}_{i,j},\ \nabla V^{\mathrm{MAP}}_{i,j}\right)$ of the local diffusivity and force field are the Maximum a Posteriori (MAP) of the posterior distribution of the parameters.

Potential optimization from the gradient field. The potential at the surface of the cell is extracted from the MAP values of its gradient field. The estimation is performed by minimizing $\xi(\{V_{i,j}\})$, which is defined as

$$\xi\left(\left\{V_{i,j}\right\}\middle|(i,j)\in\left\{\left|N(i,j)\right|\neq 0\right\}\right)=\sum_{(i,j)}\left(\nabla V_{i,j}-\nabla V^{\mathrm{MAP}}_{i,j}\right)^2+\beta(\delta)\sum_{(i,j)}\left(\nabla V_{i,j}\right)^2 \qquad \text{(S9)}$$

with |N(i,j)| the number of neighboring occupied mesh domains, β(δ) a constant (optimized on numerically generated trajectories) depending on δ that is the ratio between the size of the domains and the average length of the protein motion during Δt. In order to diminish the bias that the mesh could induce in the evaluation of $\nabla V_{i,j}$, the gradient along the two directions x and y was fitted, using two neighboring sites, by parabolic functions $\Im_x(x,y)$ and $\Im_y(x,y)$ so that $\nabla_x V_{i,j}=\partial\Im_x(x,y)/\partial x$ and $\nabla_y V_{i,j}=\partial\Im_y(x,y)/\partial y$. $\xi(\{V_{i,j}\})$ is the sum of two terms: the first one aims to minimize the difference between the gradient of the potential field and the inferred gradient field while the second one penalizes the strong gradients. This penalization allows better convergence towards the true value of the potentials; it also prevents anomalous generation of very high potential areas that would modify the potential on a large scale.

We emphasize that typical experimental trajectories lead to several hundred to thousands of variables. The quality of the optimization on such a large number of variables was investigated numerically. Typical procedures, similar to the ones used in [5-9], have been employed to test the convergence and the quality of the inference. Here we discuss the choice of β(δ). Numerical simulations with the same diffusivities, the same average number of points per mesh rectangle, the same average trajectory duration and globally the same potential energy landscape were used to generate trajectories that were subsequently inferred for various values of β. The optimal β was the one that minimized the average square difference (ψ) between the input and the inferred potential field.

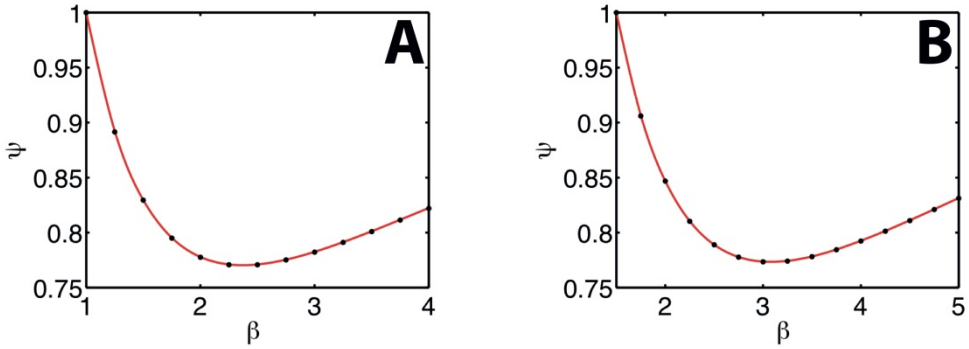

*Figure S2. **A)** Evolution of the average difference ψ (normalized here) between the theoretical potentials and inferred ones with β for a mesh subdomain with δ=2. **B**) Evolution of the average difference ψ (normalized here) between the theoretical potentials and inferred ones with β for a mesh subdomain with δ=3.*

β was found to mainly depend on the choice of δ, which in our experiments was always set between 1 and 3 to minimize the number of holes in the mesh structure. Note that the choice of β may also be driven by the search of some specific structures in the potential field, low values of β would favor large local variations of the potential whereas high values favor low variations over large scale and damp the large local variations of the potential.

Inference applied to a synaptic cluster. When dealing with local motion (*i.e.* inside a cluster), the inference scheme was derived from the ones introduced in [5-8]. Trajectories entering the synaptic area, identified as the translocations entering the fluorescent signal of the tagged gephyrin, were grouped together to be analysed. The potential was developed on a basis of function so that the inference is performed on the coefficient of the development. A simple polynomial basis provided good results (see refs [5-9]):

$$V_{2D}(x,y) = \sum_{l+m\le N} \alpha_k (x-x_c)^l (y-y_c)^m \tag{S11}$$

with (x_x, y_c) the ~~barycenter~~ center of mass of the trajectory points, $k = \frac{(l+m)(l+m+1)}{2} + l$ and N the order the polynomial. The posteriori reads:

$$\begin{aligned} P\left(\{\alpha_k\}_{k=0..\frac{N^2+3N}{2}}, \{D_{i,j}\}_{(i,j)=(1..n_x,1..n_y)} \middle| \{T_l\}\right) &= \left(\prod_{(i,j)=(1..n_x,1..n_y)} P\left(\{\alpha_k\}_{k=0..\frac{N^2+3N}{2}}, D_{i,j} \middle| \{T_l\}\right)\right) \times P(\nabla V, D) \\ &\propto \prod_{(i,j)=(1..n_x,1..n_y)} \prod_{\mu \mathbf{r}_\mu \in S_{i,j}} \frac{\exp\left(-\left(\mathbf{r}_{\mu+1} - \mathbf{r}_\mu - D_{i,j}(\nabla V)_{i,j}\Delta t / k_B T\right)^2 \Big/ 4\left(D_{i,j} + \frac{\sigma^2}{\Delta t_\mu}\right)\Delta t\right)}{4\pi\left(D_{i,j} + \frac{\sigma^2}{\Delta t}\right)\Delta t} \times \frac{D_{i,j}^2}{\left(D_{i,j}\Delta t + \sigma^2\right)^2} \end{aligned} \tag{S12}$$

With $S_{i,j}$ the mesh rectangle *(i,j)*, μ the index where the biomolecule is in *(i,j)*, Δt the acquisition time. Each mesh rectangle was treated independently and they were coupled together by the potential polynomial development. In the numerical implementation of the scheme, positions were expressed in μm, the diffusivity in $\mu m^2 s^{-1}$ and the potential in $k_B T$. Theoretically, the choice of the optimal order of the polynomial is made by comparing, for varying value of N, the evidence of the model. As the order increases, the space of integration gets larger. Due to the shape of the posteriori (product of Gaussians) integrals may be approximated by the Laplace method, *i.e.* the posteriori is approximated by a Gaussian probability distribution centered on the MAP and so the integral is evaluated directly. Yet, in a practical manner, the algorithm runs fast and so the criterion to choose the order of the polynomial may simply be the absence of change in the potential shape and the lowest error on the coefficient of the development.

Note that simple polynomial development is not the only possible basis. Depending on the type of motion and on the global geometry of the trajectory, 2D Fourier series and 2D orthogonal Hermitte functions are useful bases. The latter is interesting when dealing with local confinement surrounded by free motion. Yet, both are much less versatile in their use than the simple polynomial basis.

Error estimation. An estimate of the error on the various parameters can be obtained using one of the two following general strategies: first, the direct sampling of posterior distribution using Monte Carlo algorithm and second the evaluation of the eigenvalues of the log-posteriori Hessian at the MAP values. The latter method takes advantage that most of the relevant quantities are extracted from the neighborhood of the maximum of the distribution. However, the

Hessian, which is much faster to compute than the Monte Carlo Algorithm, will tend to slightly over-estimate the noise of the diffusivities. Furthermore, if one is interested in the error evaluation for the difference of potential between two points, Monte Carlo sampling of the posteriori is the more efficient way.

Initialization of the parameters before optimization. In the two inference schemes, the potential and the diffusivity fields have to be initialized to accelerate the convergence of the optimization processes. When the inference is performed on large surfaces, the potential is initialized by the thermal equilibrium values, *i.e.* $V_{i,j} = -k_B T \log\left(N_{i,j}/N_{Max}\right)$ with $N_{i,j}$ the number of points in the mesh subdomain *(i,j)* and N_{Max} the maximal number of points inside one of the mesh subdomains. The diffusivity fields can be initialized in two ways leading to approximately the same computation time. The most common consists in approximating the diffusivity along the arbitrarily defined x-axis and y-axis as $D_x = \left\langle l_x \right\rangle^2 / \Delta t$ and $D_y = \left\langle l_y \right\rangle^2 / \Delta t$ with $\left\langle l_x \right\rangle$, $\left\langle l_y \right\rangle$ that are the average step sizes along x and y during Δt. Then, the diffusivity field is initialized to $D_{i,j} = 1/3\left(D_x + D_y\right)$. The other one consisted on performing the same calculus but locally on groups of mesh subdomains. When the inference is performed locally, the diffusivity field is initialized in the same manner as for the inference on large surfaces. The coefficient of the polynomial development of the potential are initialized on an harmonic approximation of the potential with the spring constant $k = 2V_0 \big/ \left|\mathbf{r}_{\max} - \mathbf{r}_{mean}\right|^2$ with $\mathbf{r}_{mean}$ the average position, $\mathbf{r}_{\max}$ the position corresponding to the largest distance from $\mathbf{r}_{mean}$ and V_0 a user defined potential value, usually set to $5k_BT$.

Possible bias during the potential landscape optimization. Here, we want to emphasize an important point. In all the possible applications of the different schemes shown here, it is essential to quantify their behaviors with extensive simulations. Furthermore, most of the bias that we have encountered (see for example [7,8]) can be analytically corrected. Fortunately, the overdamped Langevin equation framework is fast to simulate, allowing direct testing of the various types of inference schemes. Theoretically, the quality, the rate of convergence and the optimality have to be evaluated by computing the Fisher Information [2,3]. Unfortunately, in most of these systems, the summation over all possible parameters state is impossible due to its large size. Hence, we have to rely on extensive simulations to study the behavior of the inference.

In order to illustrate the bias that can appear on the potential maps, we show on the next figure an example of complex field inference. As an example of complex field, we chose an oscillating potential because it induces a very incomplete sampling of space due to the proximity of low potential region to high potential region:

$$V(\mathbf{r}) = k_B T\left(2 + \cos\left(\frac{2\pi}{\lambda}x\right) + \cos\left(\frac{2\pi}{\lambda}y\right)\right) \tag{S13}$$

with λ=800 nm. The inferred potential (Fig S3. A,B) matches the structure and the amplitude of the potential used to generate the trajectories. The advantage of using symmetric potential fields is that it highlights (by propagating them) the defects of the optimization procedure. Interestingly, the potential is well inferred near the boundaries of the domains,

while in some parts near the center, there are small differences between the inferred and the simulated potential but these errors do not propagate thanks to the damping term $\beta\left[\vec{\nabla}V(\mathbf{r})\right]^2$ in the optimization function. Overall, the inference is able to recover fast variation of the potentials with local bias near high potential structures.

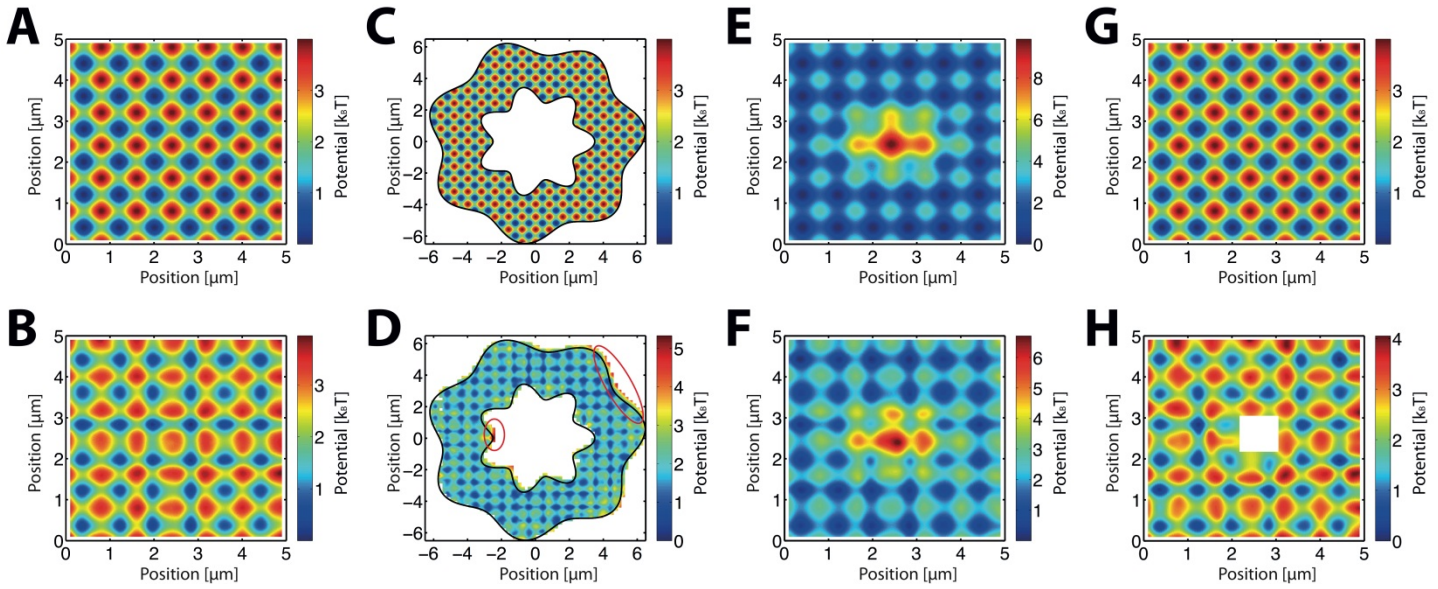

*Figure S3. **A)** Potential map used to generate the trajectories. **B)** The inferred potential field with trajectories simulated in **A**). **C)** Potential map used to generate the trajectories. **D)** The inferred potential field with trajectories simulated in **C**). The red ellipses point the two local areas where there is a significant bias. Simulations to generate the trajectories were made with reflecting boundary conditions on the borders, shown here by the black curves. **E)** Potential map used to generate the trajectories. **F)** The inferred potential field with trajectories simulated in **E**). **G)** Potential map used to generate the trajectories. **H)** Inferred potential field with trajectories simulated in **G**). The white square is the un-sampled part of space due to the removal of the trajectory points. Simulations are performed with a diffusion field with constant value $D=0.1\mu m^2 s^{-1}$ and $\Delta t=50ms$. Note that the colorbar may be different between the simulated and inferred landscape.*

More generally, the borders tend to generate limited or very localized bias. In Fig.S3C,D we show on a complex geometry (with an identical potential as the one used in Fig.S3A,B) that the borders do not shift significantly the inferred potential from their true values in the internal part of the maps, and that mainly on the top right of the geometry, in a region mostly unvisited the potential is locally biased. In most parts of the border regions there are no biases in the inferred potentials. Note that the differences in the color of the maps are induced by the high potential region on the top of Fig.S3D. The inference is not going to detect every possible structure. Obviously, diffusion or interaction structures on scales largely inferior to the scale of the diffusion motion ($\sim\sqrt{4D_{i,j}\Delta t}$) cannot be seen. Note that it does not mean that other estimators could not be used to extract characteristics of these structures, yet in order to access these scales prior knowledge would be necessary. One of the key interests of the mapping scheme is that no prior information is needed to extract information from the random motion. Some structures of potential are also going to shield others from being accessible to the inference. In Fig.S3E,F we show an example on a more heterogeneous potential. The potential is well inferred except in the region of high potential that is partially inaccessible due to its high value. Yet, the average

difference between local maxima and minima of the potential, in the periodic structure, is the theoretical value (4 k_BT). This proves that some potential structures can prevent the inference from accessing local information but that this will not have large scale effects. Finally, some regions may be unvisited for technical reasons such as regions that are out of focus or simply the absence of experimental points. In Fig.3G,H we show the effect of un-sampled areas by removing all the points in the trajectories inside a square. We made the empty square larger than the ones met experimentally to induce a noticeable effect. Again the inference is slightly biased near the anomaly (lack of points) but remains of good quality on the rest of the surface. There are no biases in the estimation of the difference between the maxima and the minima of the potentials (4 k_BT).

Finally, we tested the inference scheme in the absence of potentials to ensure that optimization on large surfaces did not generate local potentials (this test had already been performed for the confined trajectories in local potentials [7,8]).

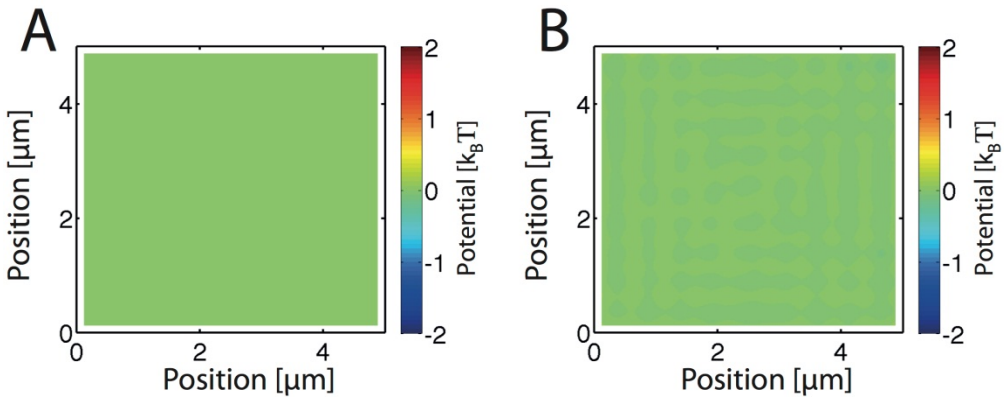

Figure S4. A) Constant potential used to generate trajectories. B) Inferred potential. Note the low values of the potential value; the noise in the potential is 0.15 k_BT; it is the consequence of the mesh with small variation of potential near neighboring mesh subdomains.

Some of the possible structures that may appear when there is a constant potential are small oscillations of potential values between neighboring mesh subdomains. They are mostly the consequence of the finite mesh size. Yet, if experimentally we would expect small potential values or large areas without potentials variations, the value of β should be raised. Another possible way to deal with flat regions and other possibly complex structures would be to build non-regular types of mesh. Meshes generated to have identical number of trajectory points lead to very good results by diminishing the bias in the inferred potential. Yet, the relations between the numbers of points in each mesh subdomain, the characteristics of the potential and diffusion landscape and the value of β are less direct than for regular meshes. In Fig.S5, we show an example of these structures in the experimental energy landscape for the β^--TM construct

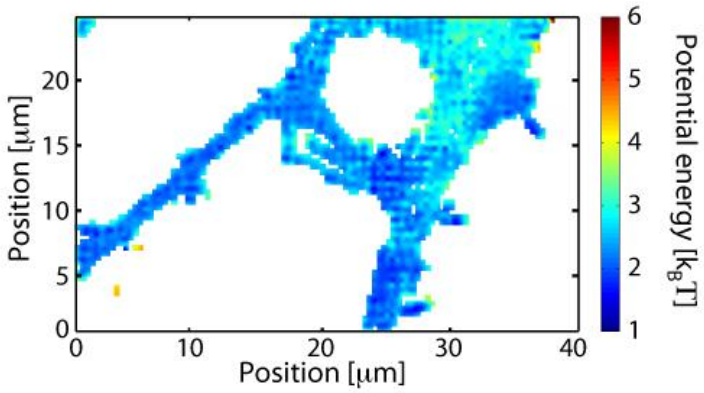

Figure S5. Energy Maps for membrane construct β-TM.

2. **Simulations and measurements in the landscapes**

Why performing Simulations in the Maps. Probing a biological environment using single molecule technics (SPT, PALM, UPaint etc.) involve a tradeoff between 3 main phenomena:

- Spatial Sampling
- Duration of Recording
- Typical time of biological variations

Efficient spatial sampling, especially for large areas (>1μm^2), can either be achieved by long trajectories or by numerous short trajectories. It is also worth noting that the nature of the motion (fractional Brownian Motion, Continuous Time Random Walk etc.) may prevent efficient spatial sampling. Precise measures of temporally averaged estimators (MSD, first time passage) require long trajectories to be discriminative. Yet, the possible heterogeneities of the surrounding media are going to be inserted in the estimators preventing their direct use as parameters estimators or as model discriminant. Finally, All measures have to be made with minimal variations of the biological system. Again, it is worth noting that in most biological systems all the characteristics times of biological variations are not known, hence measures based on the fluctuations of interests estimators are useful to detect significant variations of the biological system.

In order to analyse, at multiple scales, the neuronal membrane, we combined the UPaint recording, the inference scheme and the simulations in the maps. Large numbers of short trajectories allow efficient space sampling even for complex media. Short individual recordings prevent the use of estimators on individual trajectories. The total time of recording (few minutes) does not lead to significant changes in the measures (done by the inference). The inference allows the measure of the diffusion and potential field on the membrane. Hence, we have shifted the balance towards space mapping and short time recording. Simulations in the maps allow studying any estimator without limitations in time or in number of trajectories. Furthermore, they allow the use of “Ensemble Averaged” estimators that are more selective than temporally estimated estimators.

Simulations in the landscapes. The maps of the diffusion and energy landscapes, D(r) and V(r), can be used to simulate the behavior of the molecules at different time and space scales. In each mesh sub-domain *(i,j)* a diffusivity $D_{i,j}$ is associated with a potential energy value $V_{i,j}$. The dynamics of the molecules are described by the Fokker-Planck equation:

$$\frac{\partial P\left(\mathbf{r},t|\mathbf{r}_0,t_0\right)}{\partial t} = -\nabla \bullet \left(-\frac{\nabla V(\mathbf{r}) P\left(\mathbf{r},t|\mathbf{r}_0,t_0\right)}{\gamma(\mathbf{r})} - \nabla\left(D(\mathbf{r}) P\left(\mathbf{r},t|\mathbf{r}_0,t_0\right)\right)\right) \tag{S14}$$

where $P\left(\mathbf{r},t|\mathbf{r}_0,t_0\right)$ is the conditional transition probability from ($\mathbf{r}_0$,t_0) to ($\mathbf{r}$,t). Fokker-Planck equations can always be approximated by Master equations:

$$\frac{dP_{(i,j)}(t)}{dt} = \sum_{(i',j')\in\mathcal{N}(i,j)} W_{(i,j),(i',j')} P_{(i',j')}(t) - \sum_{(i',j')\in\mathcal{N}(i,j)} W_{(i',j'),(i,j)} P_{(i,j)}(t) \tag{S15}$$

with in our case

$$W_{(i,j),(i',j')} = \frac{D_{(i',j')}}{\Delta x^2} \exp\left(-\frac{\Delta x F^x_{(i,j),(i',j')}}{2\gamma_{(i',j')} D_{(i',j')}} \right) \tag{S16}$$

if the transition happens in x direction and

$$W_{(i,j),(i',j')} = \frac{D_{(i',j')}}{\Delta y^2} \exp\left(-\frac{\Delta y F^y_{(i,j),(i',j')}}{2\gamma_{(i',j')} D_{(i',j')}} \right) \tag{S17}$$

if the transition happens in the y direction and with $W_{(i,j),(i',j')}$ the transition rate from the *(i',j')* site to the *(i,j)*, Δx (Δy) the mesh size in the x (y) direction, and $F^{x(y)}_{(i,j),(i',j')}$ the potential gradient acting on the random walker in the x (y) direction when moving from *(i',j')* to *(i,j)*. The motion of the molecule following equation (S19) was simulated using the Gillespie scheme [10]. When the molecule was at the site *(i,j)*, the transitions rates, rewritten a_υ to match Gillespie formalism, υ taking values from 1 to 4, were evaluated on all neighboring sites. We define $a_0=\Sigma_\upsilon a_\upsilon$. The time, τ, to move from the site *(i,j)* to a neighboring site is extracted from an exponential probability density function of rate a_0, so that

$$\tau = \frac{1}{a_0} \log\left(\frac{1}{r_1}\right) \tag{S18}$$

with r_1 a random number in [0,1]. The destination site, k, is chosen to satisfy

$$\sum_{\upsilon=0}^{k-1} a_\upsilon \le r_2 a_0 < \sum_{\upsilon=0}^{k} a_\upsilon \tag{S19}$$

with r_2 a random number in [0,1]. Limits of the neuronal cells and unvisited sites are defined as inaccessible sites. Note that the trajectory generation process leads to trajectories with non-constant time steps. In order to evaluate the different estimators (see below), trajectories were regularized to obtain the molecule position at regular time lags by imposing that as long as each τ was not reached the molecule did not move.

Computations of the estimators of the protein movement. Here, we explain how the various estimators of the protein movement were extracted and also show other possible estimators that were not included in the main text. Unless mentioned otherwise, the estimators were obtained by averaging trajectories coming from different neuronal maps or from different clusters. Using the simulated data, we computed:

- The propagator $\Pi(d,t)$, *i.e.* the probability of moving a distance d in a time t.
- The scaling factor $\chi(t)$ (Fig.4c), computed from $\Pi(d,t)$
- The ensemble-averaged mean squared displacement (MSD) defined as

$$\left\langle \mathbf{r}^2(t) \right\rangle = \frac{1}{N}\sum_{i=1}^{N}\left(\mathbf{r}_i(t)-\mathbf{r}_i(0)\right)^2 \tag{S20}$$

with N the total number of trajectories.

- The time statistics to escape gephyrin clusters (Fig.S6A), computed by generating trajectories beginning in the clusters and measuring the time needed to exit the clusters.

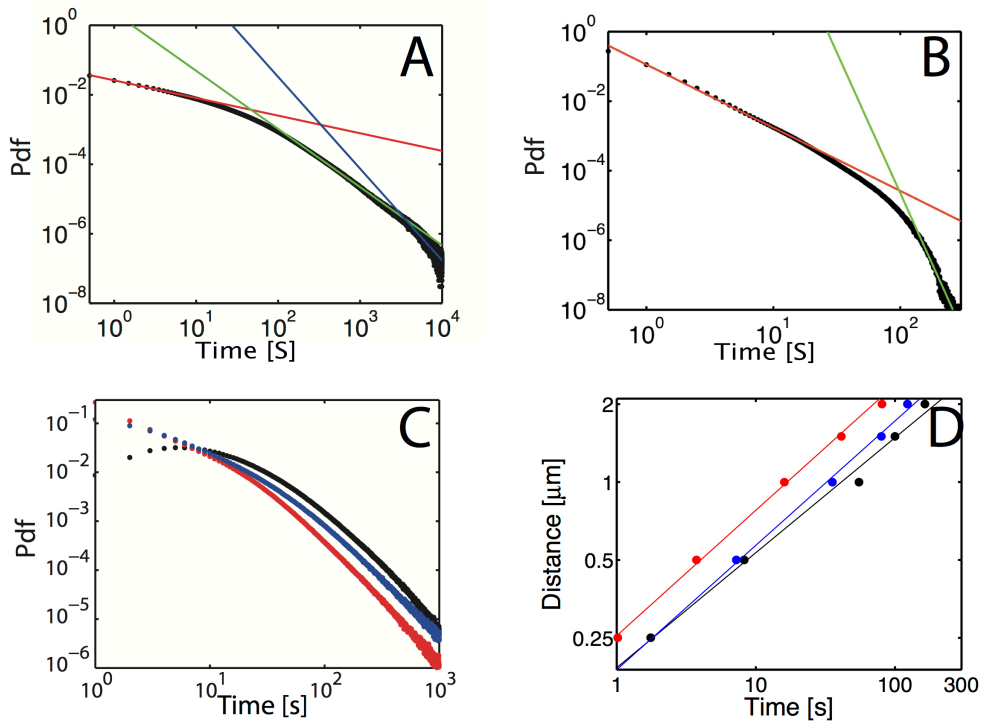

*Figure S6. **A)** Example of "time to escape gephyrin clusters" statistics based on simulations on subsets of β^{WT}-TM molecules, shown in log-log scale. Black points are results of simulation and colored lines are linear fits (in log-log) with slope α=-1.8 in red and in α=-8. in green. **B)** Example of "time to reach a gephyrin cluster" statistics based on simulation on subsets of β^{WT}-TM expressing neurons in log-log scale. Black points are results of simulation and colored lines are linear fits (in log-log) with slope α=-0.5 in red, α=-1.7 in green and α= -2.6 in blue. **C)** Statistics of first time passage for a distance of 1µm, average over the complete set of neurons. Colors are associated to receptors, β^{WT}-TM in black, β^{S403D}-TM in Blue and β^{-}-TM in Red. **D)** Evolution of the distance that receptors first reach with the average first time to reach it. Colors are associated in the same fashion as for **C)**. the distance scales as t^{η} with η=0.44 for β^{WT}-TM, with η=0.48 for β^{S403D}-TM and with η=0.49 for β^{-}-TM.*

- The time statistics to enter a gephyrin cluster (Fig.S6B), computed by measuring the time needed to get to a cluster, starting from any point outside of clusters.
- The first passage time statistics to reach a specific distance (Fig.S6C), computed by generating trajectories starting from any point at the surface of the neuron and measuring the time needed to reach the defined distance for the first time.

- The evolution of the distance to reach with the average first time to reach it (Fig.S6D), computed from the first passage time statistics.

Simulations of the fluctuations of receptor numbers. Fluctuations of the number of receptors in the gephyrin clusters were (numerically) measured by placing receptors at the surface of a neuron with experimentally measured densities, *i.e.* 500 receptors per μm^2 inside gephyrin clusters and 5 receptors per μm^2 outside, and then letting them evolve using the Gillespie scheme. We thus deduced the time course of the number of receptors at individual synapses (see results in Fig.4). Using the same method, we also computed a map of relative variations of receptor numbers (Fig.S7).

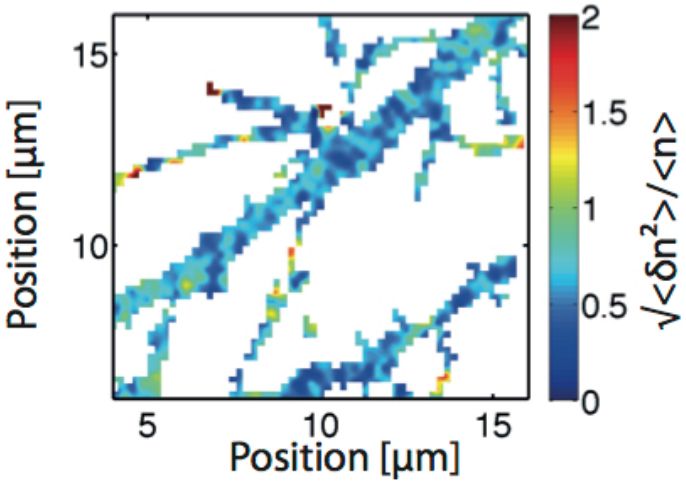

Figure S7. Map of the relative variation (standard deviation over mean) of receptor number during a 100 s temporal window.

3D Biases. The inference scheme is not limited to 2D motion and may be applied in 3D. In our case the transmembrane proteins movements were analyzed in 2D although the membrane can exhibit curvature. However, we show that the possible local curvature of the membrane has a limited effect on the inferred values.

We first simulated the random walk on a cylinder with high curvature $\varkappa$=4 μm^{-1} (R=250nm) and inferred the diffusivity field using the inference scheme developed in the paper. The motion was not limited along the axis of the cylinder. We show, on figure S8A, the statistics of diffusivity values inside all mesh squares

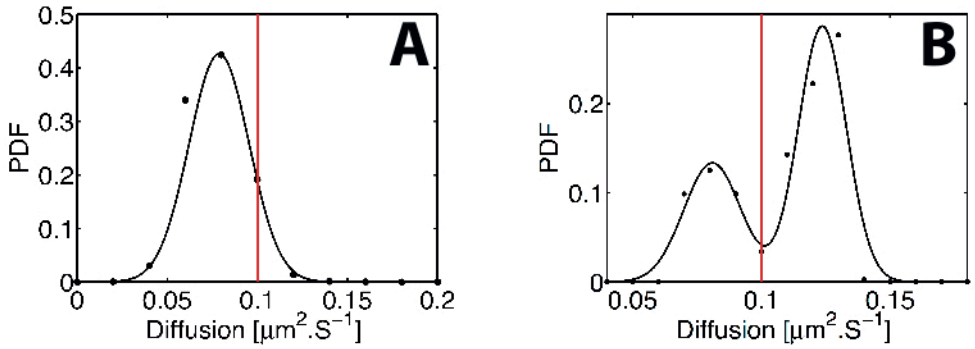

Figure S8 . Inferred diffusivity statistics of a random walker on a cylinder A) and on a sphere B) of radius 250nm with Δt=50ms. The diffusion used to generate the trajectories is D=0.1$\mu m^2 s^{-1}$ and is indicated by the red lines. Trajectories are recorded on (x,y) plane. The statistics is made with the MAP values of the diffusivity in each mesh square of the mesh.

We next simulated the random walk on sphere with high curvature $\varkappa$=4 μm^{-1} (R=250nm). Results are shown on Fig.S8B. The statistics show two local maxima centered on the true value of diffusivity, and the average value of the distribution is <D>=0.11±0.02 $\mu m^2 s^{-1}$. We observe that for high curvature the inference scheme tends to slightly shift the diffusivities. Interestingly, when there is curvature the diffusivity statistics have characteristics that differ from the ones on flat surfaces. Furthermore, the statistics of the points' positions that are concentrated on the limit of the cylinder or the sphere indicate the presence of curvature. So, here we deliberately applied the inference without taking the noticeable curvature effect (very inhomogeneous repartition of points) into account. Note that in both cases if the curvature is taken into account, by modifying the expression of the likelihood, both statistics become unbiased and centered on the true value of diffusivities.

Here, we show how to generate the trajectories on the cylinder and the sphere. The simulation of the random walk on the cylinder was straightforward because of the parameters values:

$$\begin{aligned} \theta_{t+dt} &= \theta_t + \sqrt{\frac{2Ddt}{R^2}} dU_t \\ y_{t+dt} &= y_t + \sqrt{2Ddt}\, dV_t \end{aligned}, \tag{S21}$$

with R the radius of the cylinder, θ the radial angle, y the direction of the cylinder, D the diffusivity, Δt the time between each move, and $\left(dU_t, dV_t\right)$ Gaussian random numbers of null average and of unit standard deviation.

In that case the propagator reads

$$P\left(\theta, z, t \middle| \theta_0, z_0, t_0\right) = \left[1 + \sum_{n\geq 1} \cos\left(2\pi n\left(\theta - \theta_0\right)\right) e^{-\frac{4\pi^2 D(t-t_0)}{R^2}}\right] e^{-\frac{(z-z_0)^2}{4D(t-t_0)}} \Big/ \sqrt{4\pi D\left(t-t_0\right)}\,, \tag{S22}$$

The simulation of the random walk on the sphere could not be simulated with a similar scheme

$$\begin{aligned} \varphi_{t+dt} &= \varphi_t + \sqrt{\frac{2Ddt}{R^2}} dU_t \\ \theta_{t+dt} &= \theta_t + \frac{Ddt}{R^2 \tan\left(\theta_t\right)} + \sqrt{2Ddt}\, dV_t \end{aligned}, \tag{S23}$$

Since a suitable dt would have to be such as $\sqrt{dt} \approx R^2 / \sqrt{D}$, diffusion was simulated on a shell of width *h* such that $\varepsilon = h/R < 0.01$ with reflecting boundary conditions on the inner and outer shell. dt was adjusted so that the relation $\left\langle \cos\left(\theta(t)\right)\right\rangle = e^{-\frac{2Dt}{R^2}}$ was respected. Note that another way to efficiently simulate the random walk on the sphere, or more generally on a n sphere in an n+1 Euclidian space, can be found in [11].

In that case the propagator reads.

$$P\left(\theta,\varphi,t\middle|\theta_0,\varphi_0,t_0\right)=\sum_{k=0}^{\infty}\sum_{m=-k}^{k}Y_k^m\left(\theta,\varphi\right)Y_k^m\left(\theta_0,\varphi_0\right)e^{-\frac{k(k+1)D\left(t-t_0\right)}{R^2}}, \tag{S24}$$

with

$$Y_k^m\left(\theta,\varphi\right)=e^{im\varphi}P_k^m\left(\cos\left(\theta\right)\right), \tag{S25}$$

with P_k^m the Legendre functions.

3. **Supplementary Videos**

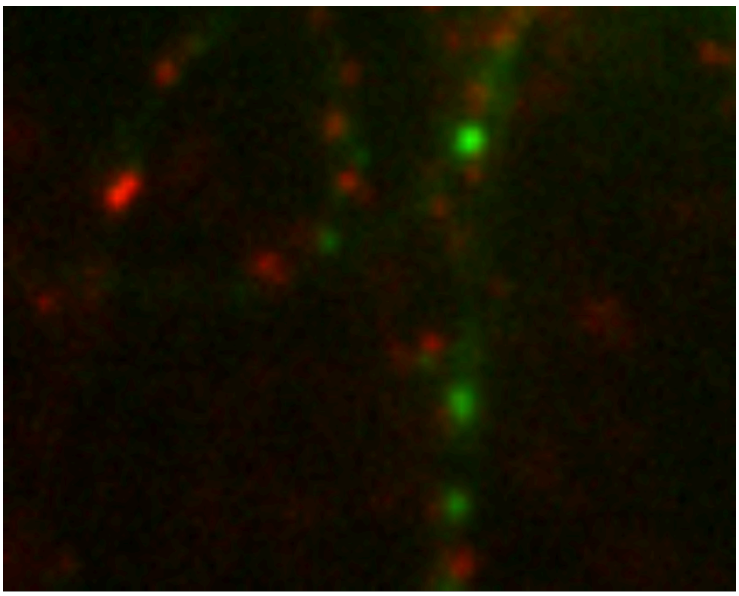

Sup Movie 1: example of a uPaint movie for the beta- TM construct (red), labeled with anti-GFP antibodies coupled to Atto647N dues, and gephyrin molecules (green). Acquisition time: 50 ms/image.

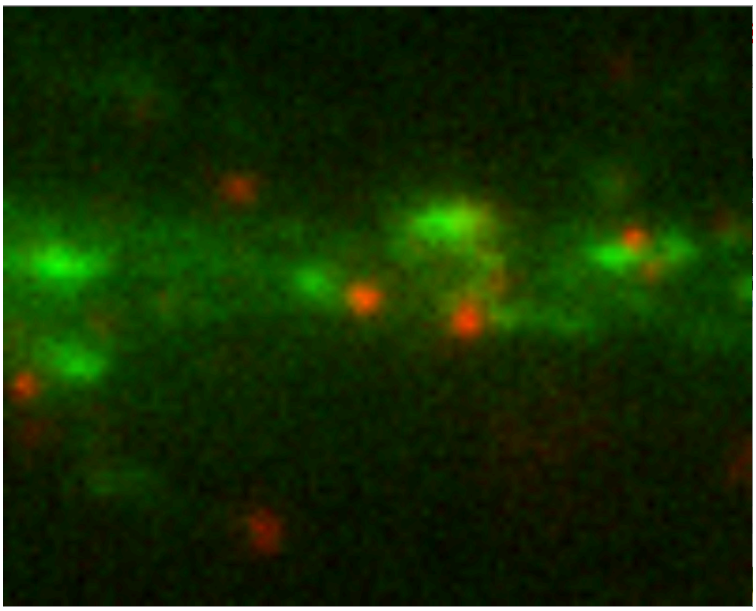

Sup Movie 2 : example of a uPaint movie for the betaWT- TM construct (red), labeled with anti-GFP antibodies coupled to Atto647N dues, and gephyrin molecules (green). Acquisition time: 50 ms/image.

References

[1] H.L. Harney, *Bayesian Inference: Parameter Estimation and Decisions*, Springer 2003
[2] D. J.C. Mackay, *Information Theory, Inference and Learning Algortihms*, Cambridge University Press 2003
[3] T. M. Cover & J.A. Thomas, *Elements of Information Theory,* Wiley Series in Telecommunication and Signal Processing 2006
[4] H. Risken, *The Fokker-Planck Equation, Methods of Solution and Applications,* Springer (1996)
[5]. Masson J-B, Casanova D, Türkcan S, Voisinne G, Popoff MR, Vergassola M, Alexandrou A (2009) Inferring maps of forces inside cell membrane microdomains. Phys Rev Lett 102**:** 048103 .
[6] Voisinne G, Alexandrou A, Masson J-B (2010) Quantifying Biomolecule Diffusivity Using an Optimal Bayesian Method. Biophys J 98: 596-605 .
[7] Türkcan S, Masson J-B, Casanova D, Mialon G, Gacoin T, Boilot J-P, Popoff MR, Alexandrou A (2012) Observing the confinement potential of bacterial pore-forming toxin receptors inside rafts with non-blinking Eu^{3+}-doped oxide nanoparticles. Biophys J, 102: 2299-2308.
[8] Türkcan S, Alexandrou A, Masson J-B (2012) A Bayesian inference scheme to extract diffusivity and potential fields from confined single-molecule trajectories. Biophys J 102: 2288-2298.
[9] Türkcan S, Richly M.U.,Alexandrou A.,Masson J.-B, *Probing membrane protein interactions with their lipid raft environment using single molecule tracking and Bayesian inference analysis,* PloS ONE 8(1): e53073
[10] Gillespie D.T., *Exact Stochastic Simulation of coupled chemical reactions,* The Journal of Physical Chemistry, 81, No 25, p2340, (1977)
[11] J. Nissfolk, T. Ekholm & C. Elvingson, *Brownian dynamics simulations on a hypersphere in 4-space*, Journal of Chemical Physics, **119**, 6423 (2003)